

THE COS-HALOS SURVEY: ORIGINS OF THE HIGHLY IONIZED CIRCUMGALACTIC MEDIUM OF STAR-FORMING GALAXIES

JESSICA K. WERK^{1,2}, J. XAVIER PROCHASKA², SEBASTIANO CANTALUPO^{3,2}, ANDREW J. FOX⁴, BENJAMIN OPPENHEIMER⁵, JASON TUMLINSON⁴, TODD M. TRIPP⁶, NICOLAS LEHNER⁷, & MATTHEW MCQUINN¹

v2.0

ABSTRACT

The total contribution of diffuse halo gas to the galaxy baryon budget strongly depends on its dominant ionization state. In this paper, we address the physical conditions in the highly-ionized circumgalactic medium (CGM) traced by O VI absorption lines observed in COS-Halos spectra. We analyze the observed ionic column densities, absorption-line widths and relative velocities, along with the ratios of N V/O VI for 39 fitted Voigt profile components of O VI. We compare these quantities with the predictions given by a wide range of ionization models. Photoionization models that include only extragalactic UV background radiation are ruled out; conservatively, the upper limits to N V/O VI and measurements of N_{OVI} imply unphysically large path lengths $\gtrsim 100$ kpc. Furthermore, very broad O VI absorption ($b > 40$ km s⁻¹) is a defining characteristic of the CGM of star-forming L* galaxies. We highlight two possible origins for the bulk of the observed O VI: (1) highly structured gas clouds photoionized primarily by local high-energy sources or (2) gas radiatively cooling on large scales behind a supersonic wind. Approximately 20% of circumgalactic O VI does not align with any low-ionization state gas within ± 50 km s⁻¹ and is found only in halos with $M_{\text{halo}} < 10^{12} M_{\odot}$. We suggest that this type of unmatched O VI absorption traces the hot corona itself at a characteristic temperature of $10^{5.5}$ K. We discuss the implications of these very distinct physical origins for the dynamical state, gas cooling rates, and total baryonic content of L* gaseous halos.

Subject headings: galaxies: halos – galaxies:formation – intergalactic medium — quasars:absorption lines

1. INTRODUCTION

Quasar absorption-line techniques have established that present-day galaxies are enveloped by a highly-ionized and enriched plasma extending to hundreds of kpc. Although largely invisible in its faint emission, this ‘halo gas’ or ‘circumgalactic medium’ (CGM) is revealed by observations of the O VI doublet at $\lambda\lambda 1031, 1037$ in far-UV absorption-line spectroscopy of background quasars (e.g. Tripp et al. 2008; Wakker & Savage 2009; Prochaska et al. 2011a; Tumlinson et al. 2011; Savage et al. 2014). Dedicated studies have assessed the covering fraction, surface density, and radial extent of this O VI-bearing gas, including its relationship to galaxy stellar mass and star formation rate. While this O VI is common around $\sim L^*$ star-forming galaxies, it appears less common around non-star-forming galaxies (Tumlinson et al. 2011) and low-mass dwarf galaxies (Prochaska et al. 2011a). It may (Tripp & Savage 2000; Shull et al. 2003; Chen & Mulchaey 2009; Stocke et al. 2014; Johnson et al. 2015) or may not (Wakker & Savage 2009) be

common in galaxy-group environments and/or intracluster gas (e.g. Bowen et al. 2001).

Recent observational studies have placed lower limits on the highly-ionized metal mass in the CGM of L* galaxies traced by O VI. It most likely exceeds $10^7 M_{\odot}$ (Tumlinson et al. 2011), comparable to or greater than the metal mass within their ISM (Peeples et al. 2014). The chief uncertainty in CGM metal-mass estimates arises from the largely unknown ionization conditions of the gas. Typically, lower limits on oxygen budgets in the highly ionized gas are derived by simply assuming that O VI is at its maximum ionization fraction in typical low-density conditions. However, the true metal budgets vary greatly depending on the model used to explain the ionization, which in turn significantly affects conclusions about the fate and origin of the highly ionized gas around galaxies.

Several authors have recently addressed the origin and total baryonic content of the highly ionized gas in the CGM by comparing simulations with observations. Strong feedback processes (from both star-formation and AGN) give rise to significant O VI absorption in the CGM of both cosmological zoom-in and hydrodynamical simulations (e.g. Shen et al. 2013; Hummels et al. 2013; Cen 2013; Suresh et al. 2015; Liang et al. 2016; Ford et al. 2016; Oppenheimer et al. 2016; Rahmati et al. 2016; Cen & Safarzadeh 2016). However, the column density of the simulated O VI absorption depends upon an assumed ionization mechanism of the gas. Just as observers must model their absorption-line data with a radiative transfer code like Cloudy (Ferland et al. 2013) to determine the physical characteristics of the gas (e.g. Werk et al. 2014), so must simulators reproduce the physical conditions in

¹ University of Washington, Department of Astronomy, Seattle, WA jwerk@uw.edu

² UCO/Lick Observatory; University of California, Santa Cruz, CA

³ Institute for Astronomy, ETH Zurich, Wolfgang-Pauli-Strasse 27, 8093 Zurich, Switzerland

⁴ Space Telescope Science Institute, 3700 San Martin Drive, Baltimore, MD

⁵ CASA, Department of Astrophysical and Planetary Sciences, University of Colorado, Boulder, CO 80309

⁶ Department of Astronomy, University of Massachusetts, Amherst, MA

⁷ Department of Physics, University of Notre Dame, Notre Dame, IN 46556

their gas cells using radiative transfer models that provide corresponding values of gas column density of a given ion. Under the standard assumption of ionization equilibrium and a combination of photo- and collisional ionization, simulators compare their model-derived radial distributions of O VI absorption with the O VI column density distributions from observations (though see Oppenheimer et al. 2016). These comparisons routinely reveal a deficit of O VI column density in the simulated gas cells compared to observations, perhaps hinting at some unaccounted for ionization process (e.g. Suresh et al. 2015).

It has thus far been difficult to generalize the physical conditions of intergalactic and/or circumgalactic gas bearing O VI despite its frequent detection and broad characterization in UV spectroscopic observations. Detailed studies have been carried out on an absorber-by-absorber basis in high-resolution and high-S/N QSO spectra that trace low-density foreground gas in the IGM and galaxy halos (Richter et al. 2004; Sembach et al. 2004; Tripp et al. 2006, 2008; Howk et al. 2009; Narayanan et al. 2010, 2011; Savage et al. 2011; Narayanan et al. 2012; Savage et al. 2014; Muzahid et al. 2015; Pachat et al. 2016). These studies have revealed the ionization mechanisms of O VI and other ‘high-ions’ like N V to be both varied and complex over a wide range of environments (e.g. Sembach et al. 2004). Line diagnostics from low, intermediate, and high ions, including ionic column density ratios and absorption-line profiles, sometimes support a similar, photoionized origin for O VI, N V, and low-ionization state gas (e.g. Tripp et al. 2008; Muzahid et al. 2015), and sometimes require O VI to be ionized by collisions of electrons with ions in a $\sim 10^{5.5}$ K plasma (e.g. Tumlinson et al. 2005; Fox et al. 2009; Savage et al. 2011; Tripp et al. 2011a; Wakker et al. 2012; Narayanan et al. 2012; Meiring et al. 2013). Often, the multiple components for a single absorber show both narrow and broad absorption lines consistent with both scenarios. A similar challenge arises from the diffuse gas known as high velocity clouds (HVCs) in the halo of the Milky Way (Sembach et al. 2003; Fox et al. 2004, 2005, 2006; Lehner et al. 2009; Wakker et al. 2012). In this case, the complex mixing and shocking of cooler gas within a hot, ambient medium is often consistent with the absorption-line diagnostics.

Here, we focus on the physical conditions of the O VI-bearing gas around $z \sim 0.2$ star-forming $L \approx L^*$ galaxies. Previous studies have focused on the Milky Way itself (e.g. Fox et al. 2004; Lehner et al. 2011; Wakker et al. 2012), on single sightlines with exquisite, high-S/N UV spectra (e.g. Narayanan et al. 2010, 2011; Tripp et al. 2011a; Narayanan et al. 2012; Meiring et al. 2013), $z \sim 2-3$ Lyman limit systems or damped Lyman α systems (Fox et al. 2009; Lehner et al. 2014), or on absorption lines originating in wide variety of galaxy or group environments (Heckman et al. 2002; Grimes et al. 2009; Wakker & Savage 2009; Bordoloi et al. 2016). The COS-Halos dataset provides a uniform sample of absorbers with well-characterized host galaxy properties that allow us to generally constrain ionization processes affecting O VI in the star-forming galaxy halo environment and potentially relate them to galaxy properties. While the COS-Halos spectra have only moderate S/N (~ 10 at O VI), they cover a wide range of transitions at $z \sim 0.2$,

including (but not limited to) Si II, Si III, Si IV, N II, N III, N V, and O VI. The coverage of such a variety of ionic species allows us to uniquely assess the multiphase nature of the gas within 150 kpc of a star-forming galaxy for 24 distinct sightlines. Ultimately, our goal is to apply the best available diagnostics from the COS-Halos dataset (Tumlinson et al. 2013; Werk et al. 2013) to the origins of the highly ionized gas in gaseous galactic halos, and from these diagnostics to draw conclusions about the gas flows driving evolution in these galaxies.

In Section 2 we describe the data and review the relevant properties of the low-ionization state gas. In Section 3, we present a detailed Voigt profile-based kinematic analysis, joint with the low-ions, of the individual O VI absorbers, and examine several significant correlations between the gas kinematics and COS-Halos host galaxy properties. Section 4 presents an analysis of the many ionization processes capable of producing a highly ionized plasma and compares their predictions with the COS-Halos data for component column densities, gas velocities, line-widths, and ratios of Si IV/O VI and N V/O VI. In Section 5, we summarize our results. Finally, in Section 6 we address several recent analytical and phenomenological models and comment on their applicability to our findings and implications for the co-evolution of the galaxy and its CGM.

2. OBSERVED GAS PROPERTIES

2.1. Data and Sample

The observations of CGM gas are taken from the COS-Halos survey, a dedicated absorption-line survey of $L \approx L^*$ galaxies at $z \sim 0.2$ (Werk et al. 2013; Tumlinson et al. 2013). The survey targeted 44 galaxies with a diversity of SFRs and morphology (Werk et al. 2012), using background quasars at impact parameters $R \approx 10 - 160$ kpc. Far-UV spectra were obtained with the Cosmic Origins Spectrograph (COS; Froning & Green 2009; Green et al. 2012) on the *Hubble Space Telescope* (PID 11598; PI Tumlinson). The data cover $\lambda_{\text{obs}} \approx 1150 - 1600 \text{ \AA}$, and are complemented by ground-based, echelle spectroscopy (Keck/HIRES) of the background quasar, long-slit spectroscopy of the targeted galaxies (and others in the field), and SDSS photometry (Werk et al. 2012).

Because the COS optics do not correct for the mid-frequency wave front errors arising from zonal irregularities in the HST primary, the true COS line-spread function (LSF) is not characterized by a single Gaussian. Instead, it is well described by a Gaussian convolved with a power law that extends to many tens of pixels beyond the line center (Ghavamian et al. 2009). These broad wings affect both the precision of our equivalent width measurements and complicate assessments of line saturation. We mediate these effects when we fit absorption lines (described in Section 3) by using the nearest wavelength grid point and convolving with the real LSF. Each COS resolution element at $R \sim 18,000$ covers 16 km s^{-1} and is sampled by six raw pixels. We performed our analysis on the data binned by three native spectral pixels to a dispersion of $\Delta\lambda \approx 0.0367 \text{ \AA}$. The resulting science-grade spectra are characterized by $S/N \sim 10-12$ per COS resolution element which has $\text{FWHM} \approx 18 \text{ km s}^{-1}$. We assume an absolute velocity calibration error due to the systematic uncertainty in the COS wavelength calibra-

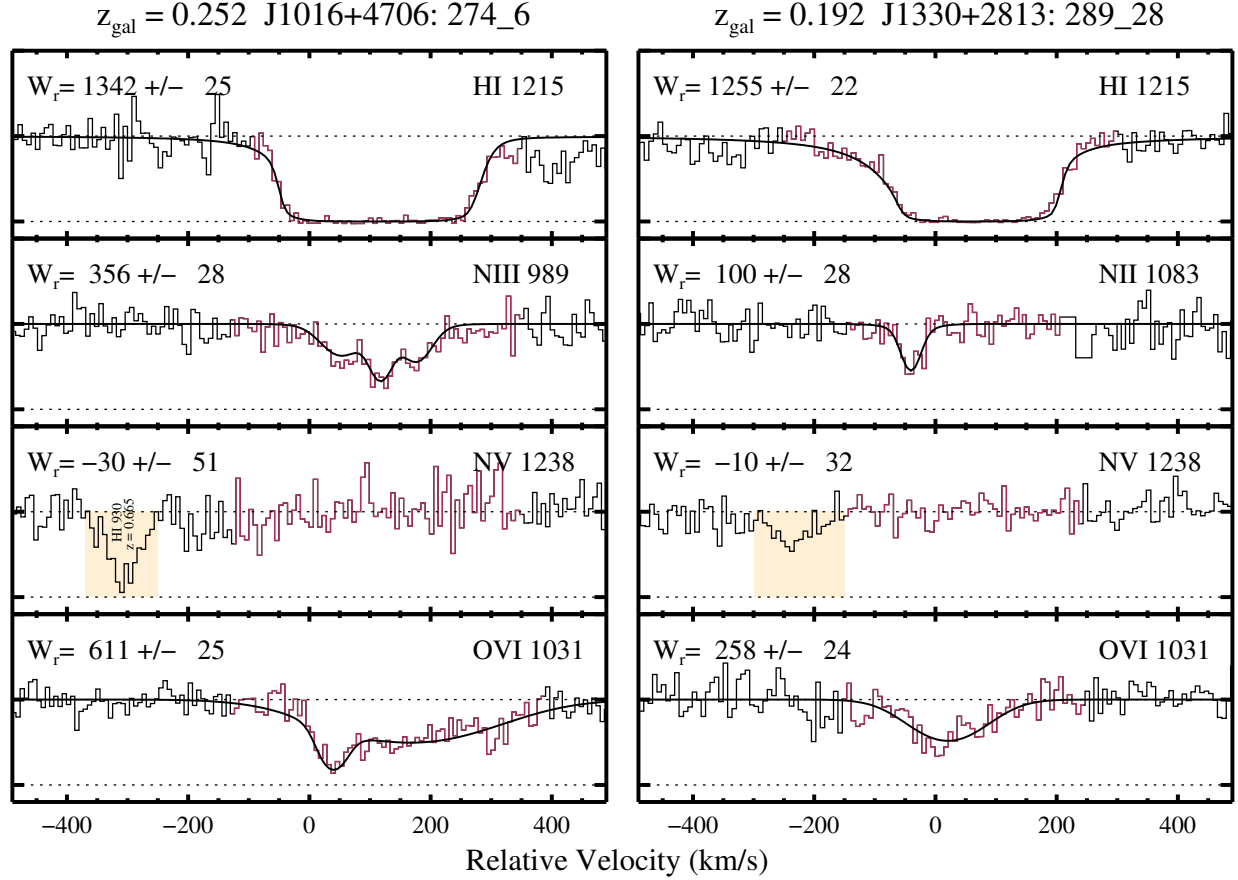


Figure 1. Ionic species stacks drawn from the *HST*/COS absorption-line spectra, centered on the transitions relevant to this study: HI Ly α , N II or N III, NV, and O VI. We show data for two representative galaxies, J1016+4706: 274.6 at $z = 0.252$, and J1330+2813: 289.28 at $z = 0.192$. In each panel, $v = 0$ corresponds to the transition wavelength at the galaxy systemic redshift. Generally, the associated CGM absorption falls within $\pm 300 \text{ km s}^{-1}$ of the galaxy systemic redshift. In both of these examples, we see strong absorption from HI, the low ionization state transitions of nitrogen, and OVI, but NV is undetected. The light shaded area on each NV panel marks a feature that is not due to NV in either case, but absorption from a system at some other redshift. For example, in the NV panel associated with J1016+4706: 274.6, this absorption line is part of the Lyman Series (H I $\lambda = 930 \text{ \AA}$) for an absorption-line system at $z = 0.665$.

tion of $\pm 10 \text{ km s}^{-1}$ (Tumlinson et al. 2013).

In this paper, we focus on the 24 star-forming galaxies that exhibit positive detections of O VI in their inner-CGM.⁸ We omit from our study the 4/13 non-star-forming galaxies that show positive detections of O VI⁹ primarily because we wish to carry out a controlled study unaffected by environmental effects; massive non-star-forming galaxies are known to live in high density environments. We additionally note that there are 2 star-forming galaxies in the COS-Halos sample that show no O VI absorption in their halos. Each is an interesting system in its own right. The first, J1550+4001 97.33, has an impact parameter of 151 kpc and shows only very broad

⁸ Officially, there is a 25th COS-Halos galaxy that would meet the criteria for star-forming host galaxy and detected O VI, J1437+5045 317.38. However, the COS spectrum of this QSO has an anomalously low S/N ($S/N \approx 4$) compared to the rest of our dataset, and we therefore exclude it from our analysis.

⁹ At least two of these systems have less-massive star-forming galaxies within 200 kpc that complicate the interpretation (Werk et al., in prep)

HI Ly α absorption (Doppler b -parameter $\approx 90 \text{ km s}^{-1}$) with $\log N_{\text{HI}} = 13.95 \text{ cm}^{-2}$. The second, J0943+0531 106.34, lies at an impact parameter of 120 kpc and has a Lyman Series down to Ly γ giving $\log N_{\text{HI}} = 15.5 \text{ cm}^{-2}$. The only detected metal ion in this sightline is Si III, and the estimated metallicity is very close to solar (Prochaska et al., in prep). The 2σ detection limit for O VI corresponds to a typical column density upper limit of $10^{13.5} \text{ cm}^{-2}$. All of the components we consider in this analysis are well-detected ($> 3\sigma$ detections).

Twenty-two of the 24 galaxies in our sample exhibit positive detections of at least one low-ionization state metal line (e.g. Si II, Mg II, C III, Si III) in addition to O VI. In every case, the COS spectra also provide spectral coverage of the N V doublet, and many have coverage of Si IV, both previously analyzed by Werk et al. (2013). Figure 1 shows two representative examples of the complete dataset. We note the strong detections of O VI and the non-detection of N V absorption despite the obvious presence of N II and N III. Of the 23 galaxies

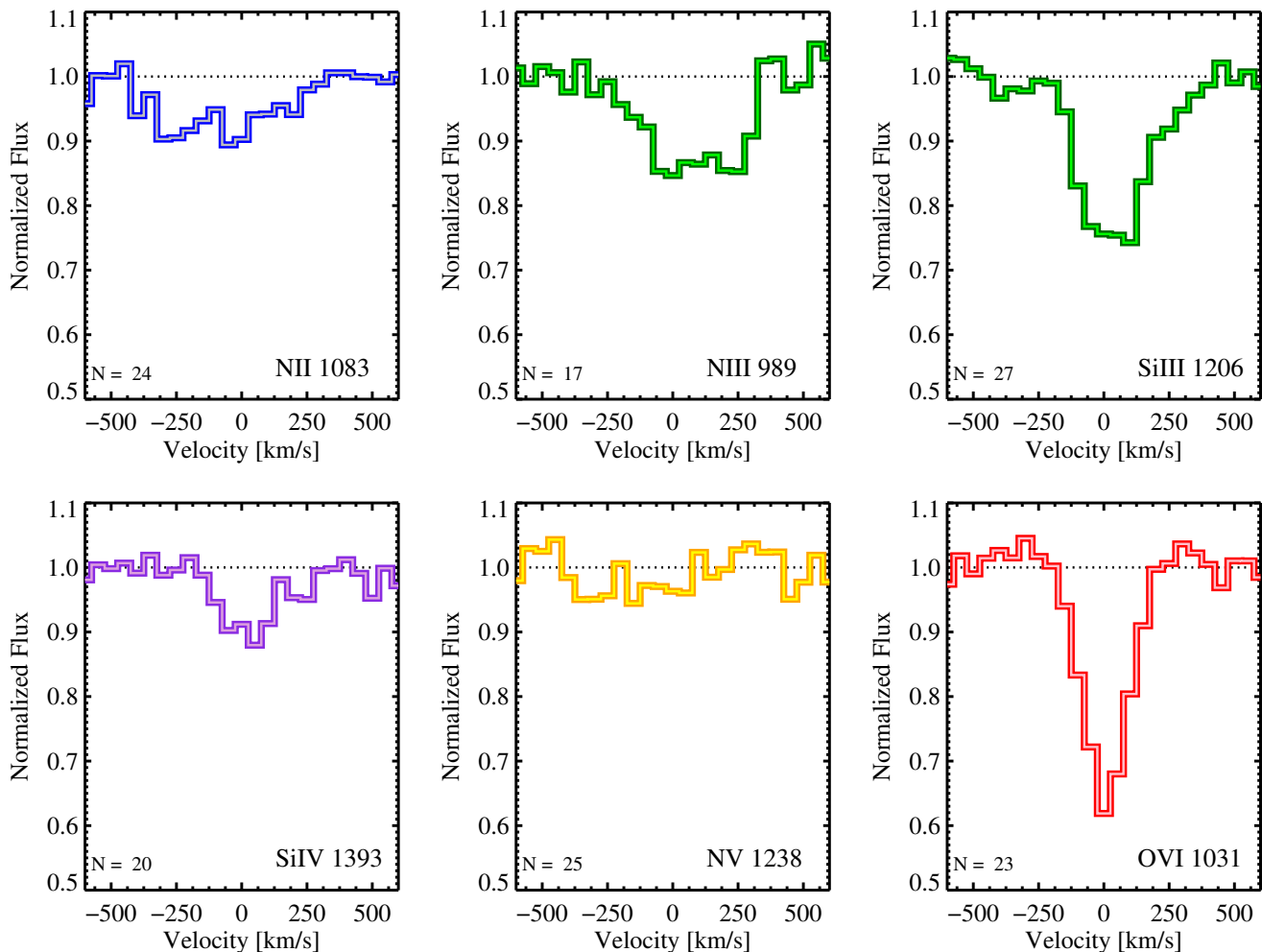


Figure 2. Average COS-Halos absorption-line spectra for NII, NIII, SiIII, SiIV, NV, and OVI, stacked at $v = 0 \text{ km s}^{-1}$ corresponding to the galaxy systemic redshift. Only the COS-Halos star-forming galaxies are included in these stacks. The resultant stacks may include coincident absorption from unrelated gas at different redshifts (or, in the case of N III 989, a neighboring transition from Si II), but this is a minor effect. The number of spectra averaged in each panel is shown in the lower-left corners. We use a spectrum if there is coverage of the transition. We note that strong absorption features (SiIII, OVI) are not driven by a small set of events, since a median stack yields qualitatively similar results.

covering both O VI and N V in COS-Halos, only 3/23 have positive detections of N V. The typical 2σ upper limits on $\log N_{\text{NV}}$ range from $13.4 - 13.8 \text{ cm}^{-2}$. Of the 19 star-forming galaxies whose COS spectra cover both O VI and Si IV, 8/19 exhibit positive detections of Si IV. These detection rates contrast with the more frequent detection of Si and N through lower-ionization transitions of Si II, Si III, N II, and N III. Table 3 of Werk et al. 2013 summarizes the constraints on the column densities for these three ions.¹⁰

Figure 2 illustrates the average absorption profiles of the sample of COS-Halos sightlines considered here. We have constructed these “stacks” by averaging the spectra in the rest-frame of each targeted star-forming galaxy (see Prochaska et al. 2013, for details)¹¹. The stacked

¹⁰ The COS spectra cover the C IV doublet in a few cases, but the S/N is too poor at its wavelength to offer a meaningful constraint.

¹¹ The resultant stacks include coincident absorption from unrelated gas at different redshifts (or, in the case of N III 989, a neighboring transition), but this is a minor effect.

profiles show strong detections of O VI absorption and also Si III, N II, and N III, consistent with the results for individual systems. On average, however, the data exhibit no detectable absorption at N V ($\lambda\lambda 1328, 1242$) and weak absorption at the Si IV ($\lambda\lambda 1393, 1402$) doublets, which have upper limits of $W_r < 100, 80 \text{ mÅ}$, respectively).

2.2. Abundance Ratios Relative to Solar Values

The non-detection of N V for the vast majority of our sightlines may indicate that the detected CGM gas is under-abundant in nitrogen, especially with respect to oxygen. The COS-Halos mean value for the *upper limit* to $\log (N_{\text{NV}}/N_{\text{OVI}})$ is -0.9 , and ranges from 0.0 to -1.9 . Ignoring ionization effects, this typical upper limit is comparable to the solar value for $\log(\text{N/O})$ of -0.86 (Asplund et al. 2009). We note that 17/39 of the COS-Halos absorbers with spectra covering both O VI and N V demand that $\log (N_{\text{NV}}/N_{\text{OVI}}) < -0.9$. As we will discuss in subsequent sections, different ionization conditions can strongly impact the conversion between log

($N_{\text{NV}}/N_{\text{OVI}}$) and $\log(N/O)$. Some models will indicate that the COS-Halos upper limits to $\log(N_{\text{NV}}/N_{\text{OVI}})$ require the assumption of anomalously low $\log(N/O)$ relative to the solar value to give physically plausible results. In contrast, other ionization models will imply that our non-detection of N V is consistent with the solar ratio of N/O for a large range of physically plausible conditions. We may use our limits on $\log(N_{\text{NV}}/N_{\text{OVI}})$ to constrain the ionization state of the gas *only* under the assumption of solar relative abundances. Here, we use independent diagnostics to examine whether the assumption of solar relative abundances in the CGM is approximately valid.

We point out that the N/O ratio is sometimes found to be sub-solar in metal-poor environments that include the ionized gas of H II regions (Henry 1993) and the neutral gas damped Ly α systems (DLAs; e.g. Reimers et al. 1992; Prochaska et al. 2002; Battisti et al. 2012; Zafar et al. 2014), sub-DLAs (e.g. Tripp et al. 2005; Battisti et al. 2012), and Lyman Limit systems (e.g. Jenkins et al. 2005). There are counter examples in which N V has been detected in analogous highly ionized absorbers along with other ions that enable the relative nitrogen abundance to be checked (e.g. SV, NeVIII, CIV, OVI). In these cases, there is no evidence of a nitrogen underabundance (Savage et al. 2002; Tripp et al. 2006, 2011b).

Figures 1 and 2 demonstrate that nitrogen is routinely detected in the COS-Halos sample, via both the N II 1083 and N III 989 transitions. Furthermore, Werk et al. (2014) found that the observed ratios of N II and N III column densities are consistent (within the 0.3 dex uncertainty) with the solar relative abundance photoionization modeling that includes low ionization states of carbon, silicon, and magnesium.

More directly, Figure 3 presents a comparison between the predicted column densities of N II and N III for the systems using the photoionization models described by Werk et al. (2014) in which the CGM is ionized primarily by the extragalactic UV background (EUVB; Haardt & Madau 2001). The resultant ionization parameters range from $-2 < \log U < -4$, values which are common for lower-ionization state gas (e.g. Prochaska 1999; Lehner et al. 2013). These models were constructed to match the constraints from all of the lower ionization states of the CGM, including the H I gas.

The y-axis of Figure 3 shows the difference between the measured ionic column densities and the column densities from the best-fitting Cloudy models presented in Werk et al. (2014). We show the data minus model differences for the low-ions most useful in constraining the solution for the ionization state of the $T \approx 10^4$ K gas: Si II, Si III, N II, and N III. Absorption lines that are saturated in the COS spectra are shown as lower limits (upward-facing arrows), while the two sigma non-detections are given as upper limits (downward-facing arrows). The models tend to simultaneously fit the many transitions of low-ion data well, with a characteristic systematic error of ± 0.3 dex. The underlying assumptions that characterize these Cloudy models are: (1) a constant gas density, (2) photoionization and thermal equilibrium, and (3) plane-parallel geometry. The systematic error is dominated by the uncertainty in the slope of the ionizing spectrum, and to a lesser extent, the departure of the elemental abundances from solar ratios. As discussed later in this paper and by Stern et al. (2016), introducing a

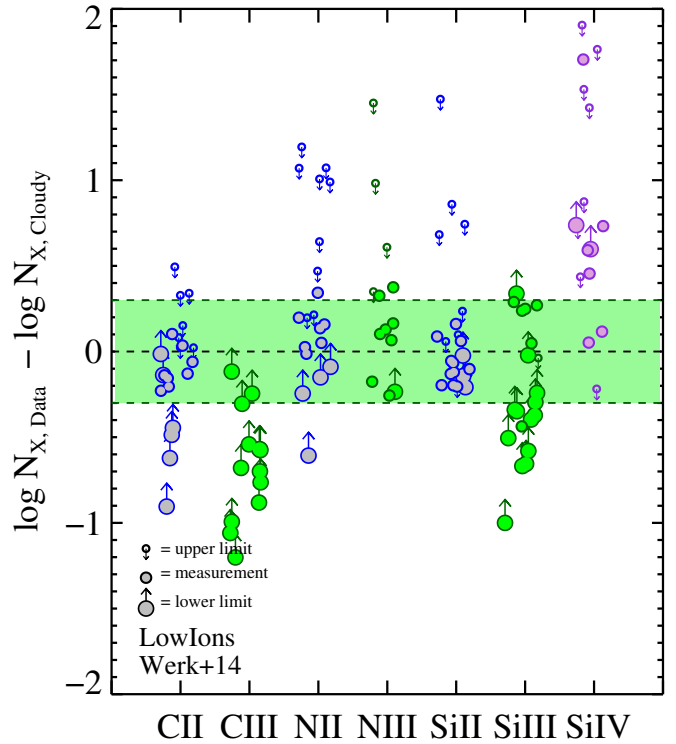


Figure 3. The difference between the measured ionic column densities and the column densities from the best-fitting Cloudy models, described in detail in Werk et al. 2014. Lower limits (indicating saturation in the absorption-line profile), are marked as the large circles with upward arrows. Upper limits (i.e. non-detection of a transition) are marked by the open small circles with downward-facing arrows. In cases where we can measure unsaturated detections, we mark the points as medium-sized filled circles. Data are color coded for the specific ionization states of the metal lines, listed on the x-axis. We consider Si IV to be an intermediate-to-high ion, and as such, the Cloudy model solutions based on the low-ions tend to underproduce the typical Si IV column densities we see in the COS data. The variety of low-ionization state transitions are consistent with solar ratios in gas photoionized by an EUVB to within ± 0.3 dex.

density gradient into the Cloudy models tends to bring the models into even better agreement with the data. In such a model, even adjacent ionization states of metal lines like Si II and Si III arise in hierarchically-nested gas clouds characterized by different densities. We note that Stern et al. (2016) assume solar ratios of the elements, and quote an uncertainty of ± 0.1 dex that accommodates possible departures from solar ratios in the COS-Halos data with their model.

Figure 3 shows broadly that these single-density photoionization models are consistent with the observed column densities of N II and N III under the assumption of solar relative abundances. Thus, anomalously low Nitrogen abundances are not necessary to explain the column densities of the low ionization state gas within the CGM. We proceed under the expectation of approximately solar relative abundances for the more highly ionized plasma traced by O VI and N V. To first order, the model predictions scale directly with this assumption.

3. GAS KINEMATICS

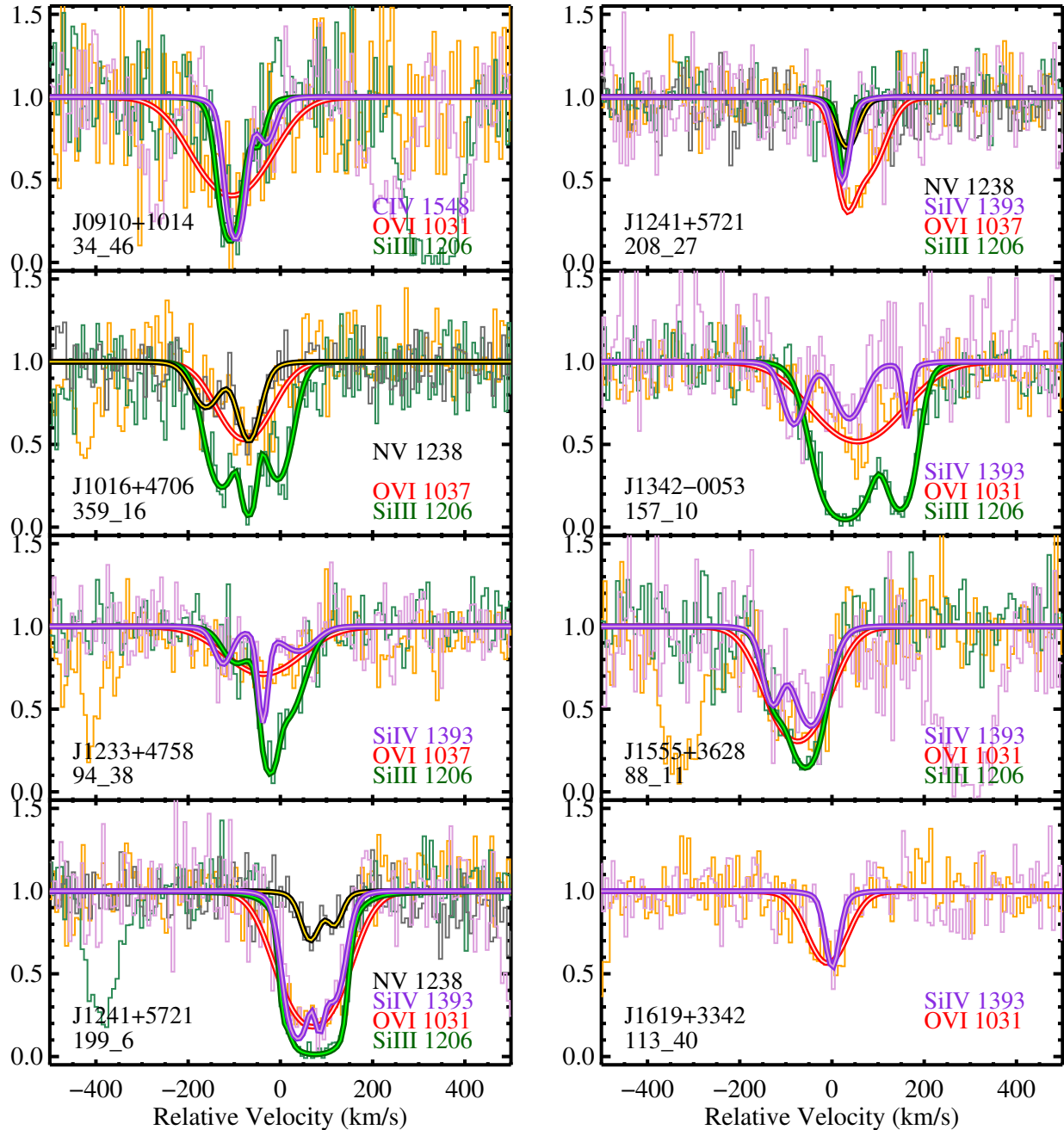


Figure 4. Comparison of continuum-normalized profile-fits for O VI (red/orange), N V, (black/yellow), Si IV or C IV (purple), and Si III (green) for 8 selected sightlines. For reference, data for each ion is shown in the same color as its Voigt profile fit. A relative velocity of 0 km s^{-1} corresponds to the systemic redshift of the associated host galaxy, determined by ground-based optical spectroscopy (Werk et al. 2012). In the lower-left corner, we provide the COS-Halos QSO name and the galaxy ID, which can be easily cross-referenced with spectra and other galaxy properties presented in previous COS-Halos papers.

3.1. The Potential for Multiple Gas Phases

Figure 3 additionally shows the difference between COS-Halos measurements and Cloudy column density predictions for the intermediate-ion Si IV using the same single-phase photoionization model as the one that matches the low-ions. This best-fitting low-ion Cloudy photoionization model under-predicts $\log N_{\text{Si IV}}$ for 6/8 detected Si IV lines by 0.5 – 1.8 dex. Werk et al. (2014) note this obvious discrepancy between the Si IV measurements and model predictions, and point out that the additional Si IV seen in the data can be explained by

invoking an intermediate-ionization gas phase. Furthermore, as one might expect, this issue is resolved by imposing a steep, inwardly-increasing density gradient on the absorbing gas cloud. The result is that Si IV represents lower-density, photoionized outer-layer gas (Stern et al. 2016).

To an even greater extent, the same discrepancy exists for O VI if we model it with the low-ions (not shown on Figure 3; it lies beyond the upper y-axis bound at > 2 dex difference). Many previous studies have recognized this need for an additional highly-ionized gas phase (Tripp et al. 2011b; Tumlinson et al. 2011; Meiring et al. 2013;

Lehner et al. 2013), and it has become common parlance to refer to the CGM as ‘multiphase’ for this reason (and others, outlined in the next section). Whether or not Si IV is in the same gas phase as O VI, or O VI represents an even lower density outer-cloud layer, is a question that we explore in later sections. Here, we simply point out the apparent excess of Si IV, and to a greater extent, O VI with respect to the predictions of single-phase, single-density, photoionization equilibrium models that include ionizing radiation from only the EUVB.

In addition to the column density ratios discussed in the previous section, several properties of CGM absorption line shapes lead to the common conclusion of a multiphase CGM. One piece of kinematic evidence for multiphases, summarized below, is the occasional misalignment of the high and low-ion absorption profiles in velocity space (see also Fox et al. 2013). Another is the systematically broader line widths of O VI absorption (e.g. Tumlinson et al. 2005; Lehner et al. 2009; Narayanan et al. 2010; Savage et al. 2011; Muzahid et al. 2012; Stocke et al. 2013). The two dominant gas phases are typically described as a cool $\sim 10^4$ K phase, and a warm, $\sim 10^{5.5}$ K phase (Tripp et al. 2008). Though we are concerned primarily with the highly ionized gas in this analysis (traced by O VI), the models we present have bearing on its interplay with the cooler gas phase traced by low (and intermediate) ionization state absorption lines. Thus, the gas kinematics of both the low and high-ions impose an important observational constraint on each of the models.

3.2. Profile Fitting and Qualitative Assessment

Tumlinson et al. (2011); Werk et al. (2013) and Tumlinson et al. (2013) summarized the COS-Halos Voigt profile fitting procedure for the O VI, the low-ions, and the HI respectively. We briefly repeat the relevant details. The procedure used to perform the fits and derive the column density N , Doppler b parameter, and velocity offset v for each component is an iterative fitting program that makes use of the MPFIT software¹². The line profiles we derive from Voigt profile fitting are convolved with the COS LSF as given at the nearest observed wavelength grid point in the compilation by Ghavamian et al. (2009). Different transitions of the same ionic species are required to have the same component structure, and are therefore fit simultaneously to give a single solution. However, we do not impose such requirements on the different ionization states of the same element. As we impose no restrictions on the component structure between different ionization states, any qualitative and quantitative similarities between the fits arise naturally.

Following (Tumlinson et al. 2013, see their Table 3), we adopt ± 10 km s⁻¹ as the systematic uncertainty associated with the first-order and higher terms of the COS wavelength solution, and thus the *relative* component velocity centroids and fitted b values. When we consider the velocity centroids relative to the galaxy systemic redshift (typical systematic uncertainty ~ 25 km s⁻¹, Werk et al. 2012), the root-square-sum gives a total error in the component velocity centroids of ± 30 km s⁻¹. Finally, we consider any line with a fitted b value of < 10 km s⁻¹ to be ‘unresolved’.

Figure 4 shows COS-Halos continuum-normalized Voigt profile fits and corresponding data for 8 sightlines that cover O VI and at least one additional intermediate or high-ionization state line, either Si IV, C IV, or N V. A qualitative assessment of the overall agreement and component structure of the low-ion (e.g. Si III), intermediate-ion (e.g. Si IV) and high-ion (O VI) lines is complex. Generally, there is good correspondence between the velocity ranges over which absorption is detected among the star-forming systems that exhibit O VI absorption (Werk et al. 2013).

Now turning to Figure 5, we show the Voigt profile fits along the sightlines (within ± 300 km s⁻¹ of the galaxy systemic redshift) of all 24 star-forming COS-Halos galaxies that exhibit detections of O VI (maroon). Where possible, we overlay Si III profiles as solid black lines, and in all cases, we show the (often saturated) HI Ly α profile fits in light gray. In this profile comparison figure, we show the continuum normalized profiles without the spectral data to facilitate a simple by-eye comparison. There are impressive alignments in component structure (e.g. J1419+4207 132.30), and occasional misalignments between the strongest absorption components of each species (e.g. J1435+3604 68.12), and sometimes O VI absorption without the presence of low-ion absorption (e.g. J1619+3342 113.40). This comparison again suggests the relationship between low and high ionization states of gas along the same COS-Halos sightlines is not straightforward. On a sightline by sightline basis, the relationship between the different ionization states can vary substantially.

Figure 5 displays a few cases in which individual components of O VI do not appear to have *any* affiliated low-ionization state metals. For example, J0914+2823 41.27 (left-hand panel, third from bottom) contains one component at -30 km s⁻¹ that shows well-matched Si III and broader, though aligned O VI, and another component at -170 km s⁻¹ that shows no Si III nor any other low or intermediate-ionization state ion. This component at -170 km s⁻¹ is *coincident* with a very broad component fit to Ly α , with $\log N_{\text{HI}} = 14.07$ cm⁻² and $b = 60$ km s⁻¹. A similar situation exists for two high-velocity ($v > 150$ km s⁻¹) components of J1112+3539 236.14. Finally, while J1435+3604 68.12 may appear to follow this trend, we note that the narrower O VI component at -60 km s⁻¹ *does* show a detection of C III (saturated, and not shown), and is embedded in a DLA system.

3.3. Quantitative Comparison of O VI and Si III Kinematics

To directly compare the absorption profile characteristics of O VI and other metal ions (e.g. Si III), we must devise a quantitative method to match various absorption features along each line of sight. We let the data drive our straightforward, observationally-motivated matching algorithm. As this analysis is focused on the highly-ionized gas, our starting point is the 39 individual fitted components of O VI along the 24 distinct sightlines within ± 300 km s⁻¹ of the galaxy systemic redshift. We attempt to match each of these individual O VI components with those of low and intermediate-ionization state species using their best-fitting velocity centroids from our Voigt profile analysis. Simply, we minimize the difference between the velocity centroids of O VI and other fitted

¹² <http://cow.physics.wisc.edu/~craigm/idl/fitting.html>

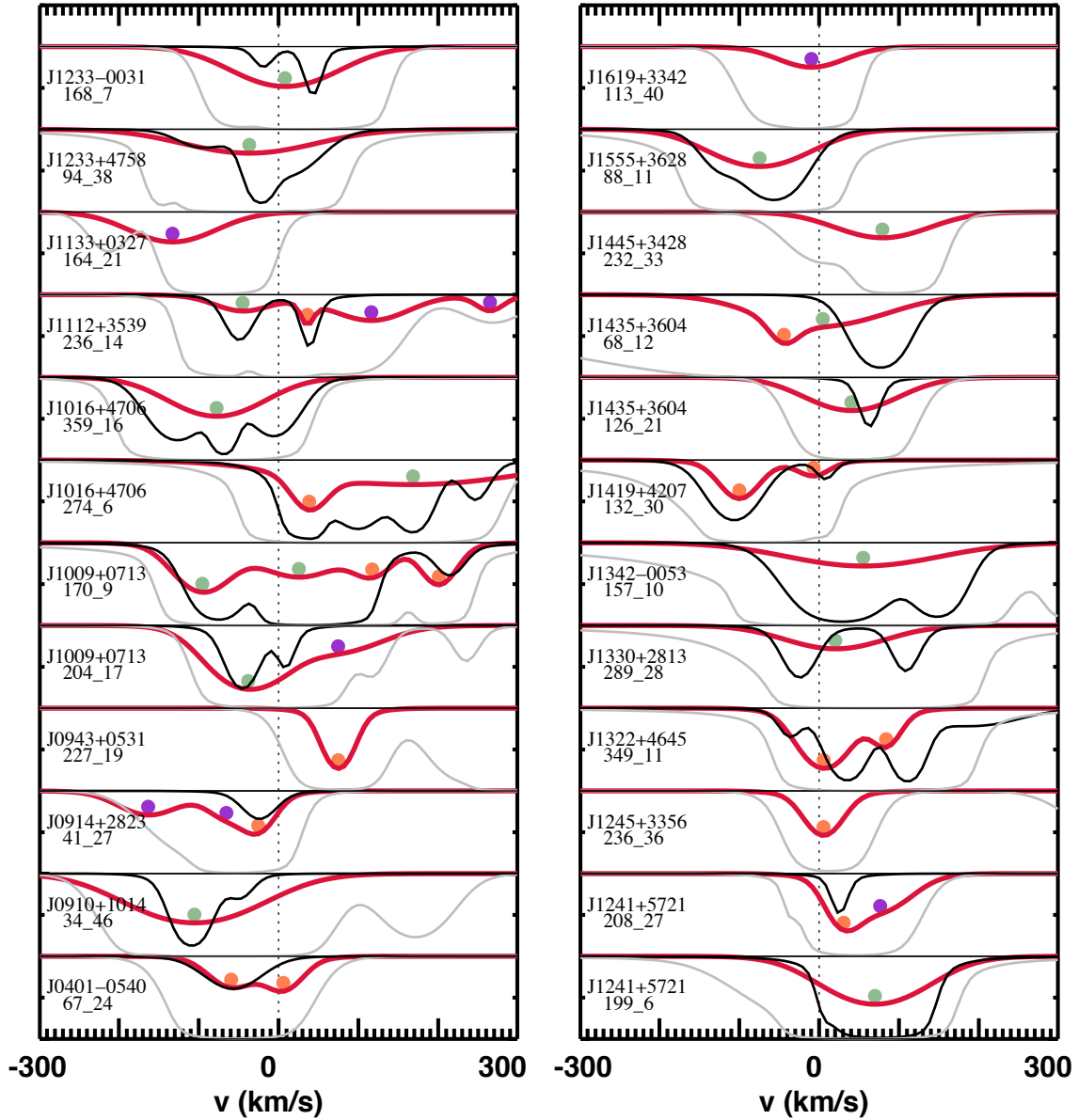


Figure 5. Comparison of continuum-normalized profile-fits for O VI (dark red), H I (gray), and Si III (black) for all 24 sightlines included in this work. On the x-axis is velocity relative to the systemic velocity of the associated host galaxy, determined by ground-based optical spectroscopy (Werk et al. 2012). To the left of the profiles, we provide the COS-Halos QSO name and the galaxy ID, which can be easily cross-referenced with spectra and other galaxy properties presented in previous COS-Halos papers. The filled, colored circles at the center of each O VI profile represent the absorption component kinematic subtypes we define in Section 3.3.1. ‘Broad’ type O VI components are colored light green; ‘narrow’ types are colored orange; and ‘no-low’ types are colored purple. This color scheme will be consistent in all subsequent figures that include the component analysis. Note that all of the orange ‘narrow’ type and green ‘broad’ type O VI absorption features have low-ion matched counterparts, though not always in Si III (Si III is generally the best covered and most often detected low-ionization state transition). The purple ‘no-low’ type O VI absorption features do not have any low-ion counterparts.

metal ion components to identify matches. We perform this test for every detected metal species and H I. Two distinct O VI components cannot have the same matching low or intermediate-ion component. The component with the best matching velocity centroid wins; the other component(s) is typically left unmatched (e.g. see the panel containing J1112+3539 236_14 in Figure 5; the purple dots mark the unmatched components).

Additionally, we set a threshold for a metal-ion match such that the difference between the values of the veloc-

ity centroids cannot be greater than 35 km s^{-1} , a limit which likely captures the wavelength calibration uncertainty of the COS spectrograph over the full COS-Halos wavelength range. Further justifying this threshold is a natural break in the distribution of component velocity centroid differences of O VI and Si III at 35 km s^{-1} . That is, there is no potential match that is rejected for a velocity centroid difference of 36 km s^{-1} ; the next closest potential match beyond 35 km s^{-1} lies at 65 km s^{-1} (see the panel containing J1009+0713 204_17 in Figure 5 for

the unmatched O VI component at 75 km s^{-1} marked by the purple dot, which is not matched with the Si III component at 10 km s^{-1} .

There are at least two major drawbacks to this method. First, matching components in this way leaves 12 low and intermediate-ion components behind because of the O VI-centric approach to matching. There are often more low-ion components than high-ion components along a given line of sight (e.g. see the panel containing J1016+4706 359_16 in Figure 5). Second, there are likely some spurious associations owing to the underlying complex velocity fields of galaxy halos (for details see Churchill et al. 2015), especially for those sightlines at low impact parameter that probe a huge range of galactocentric distances. By design, our observationally-motivated matching algorithm is well-matched to the data. This one-dimensional view, with a velocity resolution of $\sim 15 \text{ km s}^{-1}$, almost certainly does not fully capture the rich, three-dimensional physics underlying the association between low and high ion absorption. However, the benefit of this simple matching technique is that it allows us to quantify the general relationship between low and high ions discussed in the previous Section. It is our hope that being able to broadly quantify observed kinematic trends will serve to inform future physical models that aim to capture the multiphase ionization state of the CGM.

In total, there are 39 fitted O VI components in our 24-sightline sample. 31 of these components can be matched with at least one low-ionization state component (e.g. Si III) to within a velocity of 35 km s^{-1} . There are 8 unmatched O VI components. While we note that a careful inter-comparison of the H I and the O VI could be fruitful (e.g., Savage et al. 2011), it is complicated by the strong, often-saturated, and complex associated H I absorption (Tumlinson et al. 2013) that may be tracing a cooler, more neutral gas phase.

Figure 6 shows two histograms that compare the matched absorption components of Si III and O VI, the two most commonly detected metal species in the COS-Halos dataset. The two relevant absorption profile characteristics to compare are the Doppler b parameters for each ion (upper panel), and the velocity centroid differences between the matched components (lower panel). The typical errors in the b parameters from our Voigt profile analysis are $\approx \pm 20\%$. The typical errors in the fitted velocity centroids are $\pm 7 \text{ km s}^{-1}$, and thus the errors in the velocity centroids are dominated by the systematic uncertainty in the COS wavelength calibration $\pm 10 \text{ km s}^{-1}$. We note that these histograms exclude a subset of absorption-line components that cannot be matched following our procedure outlined above (8/39). We will consider this subset of the general population of absorbers separately.

In the upper panel of Figure 6, we show the distribution of Doppler b parameters for the 23 matched Si III and O VI components separately. The difference between the two ions is immediately apparent by examining the distributions of their Doppler line widths. A two-sample KS test, using the maximum deviation of 0.58, yields a probability of 0.00017 that the two b -value distributions are drawn from the same distribution. The mean line width for Si III is 22 km s^{-1} , a value typical of the

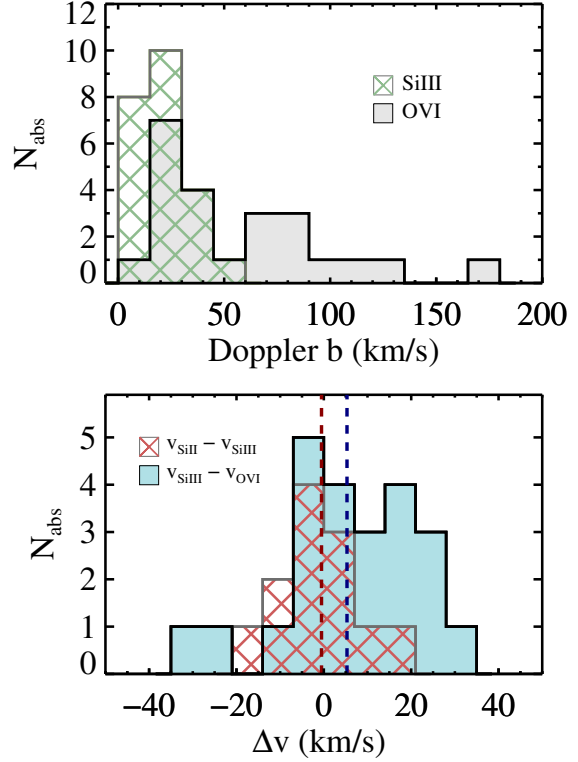


Figure 6. Upper panel: the distribution of Doppler b parameter values for matched components of Si III and O VI. Si III b values are shown in the green crosshatched histogram (mean $b = 22 \text{ km s}^{-1}$) and O VI b values lie within the gray-filled histogram (mean $b = 57 \text{ km s}^{-1}$). Lower panel: the velocity centroid differences between matched Si III and O VI absorption components (solid blue) and matched Si II and Si III components (crosshatched orange). The mean difference between the central velocities of Si III and O VI absorption is 5 km s^{-1} , marked by the dark blue dashed line, indicating O VI is typically found at lower velocities than Si III, though this is a minor effect. Comparing this Δv to that of Si II and Si III, we find the latter to be generally better matched in velocity space, with a mean of 0 km s^{-1} . For both panels, we match components based on a simple algorithm described in Section 3.3.1 that minimizes differences between central velocities of fitted components.

low-ionization state gas in COS-Halos and other absorption surveys, and comparable to the velocity resolution of COS (e.g. Savage et al. 2014; Lehner et al. 2014). In contrast, the mean line width for O VI is 55 km s^{-1} , a value that is considerably broader than the O VI absorption in general absorption-line centric surveys (discussed in Section 3.3.2; Tripp et al. 2008; Muzahid et al. 2012; Savage et al. 2014; Danforth et al. 2016).

Turning to the lower panel of Figure 6, we directly examine the differences between the velocity centroids of the matched components of Si III and O VI. For reference, we also show the velocity centroid differences between Si II and Si III. The average offset (absolute value; not shown) between our matched Si III and O VI is only 18 km s^{-1} . For the low-ions, the average offset between Si II and Si III (or C II and C III) is 7 km s^{-1} , with much greater overall agreement, and consistent with the errors in the relative wavelength scale of COS. We additionally mark the mean values of the velocity centroid differences for both pairs of ions on the lower panel of Figure 6. For offsets between velocity centroids that arise due to uncertainties in the wavelength scale and velocity resolution

limitations, we expect this mean velocity offset between components to be 0 km s^{-1} , as it is for Si II and Si III. The $5 \pm 3 \text{ km s}^{-1}$ mean value for the offsets between Si III and O VI is only marginally different from no offset at all, yet may hint that O VI sits at slightly smaller Δv (relative to galaxy systemic). Such an offset may be expected under certain physical conditions (e.g. cooling flow models) that we will explore in later sections.

For reference, two sets of unassociated absorbers distributed randomly within $\pm 250 \text{ km s}^{-1}$ would show the type of agreement between their velocity centroids seen in Figure 6 only 4 – 8% of the time. A two-sample KS-test between a random distribution of velocity centroid differences within $\pm 250 \text{ km s}^{-1}$ and the observed distribution derived from our matching algorithm shown in the lower panel of Figure 6 yields a probability of 0.0000013 that our observed component overlap is random. The association between low and high ion absorber velocity centroids is significant at a level of $\approx 5\sigma$. Furthermore, the mean difference in b values for matched components of Si III and O VI is 40 km s^{-1} . We further note that $\sim 45\%$ of matched components of the two ions show differences in b values $< 15 \text{ km s}^{-1}$ and Doppler b values $< 25 \text{ km s}^{-1}$. The b value distributions shown in the upper panel of Figure 6 reflect this dichotomy between CGM absorbers that show coincident low and high-ion absorption.

3.3.1. Identifying Three Kinematic Subtypes

Our analysis of matched and unmatched components of O VI reveals three distinct kinematic types of absorption present in the halos of star-forming L^* galaxies. Any physical picture of the CGM must incorporate all three distinct kinematic types of absorption, and is therefore likely to require multiple physical origins for O VI.

Broad: Low-ion matched O VI absorption with $b > 40 \text{ km s}^{-1}$ appears to represent 16/39 (41%) of the components. These absorbers have velocity centroids that correspond well with low and intermediate ionization state gas, but exhibit significantly broader line widths, $\Delta b > 30 \text{ km s}^{-1}$. Accordingly, we will refer to this kinematic type as ‘broad’ in subsequent text and figures; on figures it will be represented by light green squares.

Narrow: Low-ion matched O VI absorption with $b < 35 \text{ km s}^{-1}$ represents 15/39 (38%) of O VI absorbers, and is characterized by well-aligned low-ionization state components with similar line widths, $\Delta b < 15 \text{ km s}^{-1}$. We will refer to this kinematic type as ‘narrow’ in subsequent text and figures; on figures it will be represented by orange diamonds.

No-low: Finally, this third type of absorption occurs in 21% of O VI absorbers (8/39), and indicates a non-detection of low or intermediate ionization state gas within $\sim 50 \text{ km s}^{-1}$. These absorption components are typically broad, with mean Doppler b parameters of $\sim 50 \text{ km s}^{-1}$ (though two have $b < 30 \text{ km s}^{-1}$), and tend to have associated HI (within 50 km s^{-1}) with $\log N_{\text{HI}} \approx 13.4 - 15 \text{ cm}^{-2}$ and mean $b_{\text{HI}} = 40 \text{ km s}^{-1}$. We refer to this kinematic type as ‘no-low’ in subsequent text and figures; on figures this type will appear as purple circles.

We emphasize that these definitions are based purely on absorption-line kinematics and do not explicitly select for any galaxy property or absorption line column density. However, there are two possibly significant selection effects that should serve as caveats to this statement. The ‘broad’ type absorption components matched with low-ion absorption components tend to select for the highest O VI column density components. At the velocity resolution of COS, and the S/N of the COS-Halos data, the blending of narrow components separated by small offsets in velocity space (e.g. $< 10 \text{ km s}^{-1}$) is entirely possible. Thus, by selecting for broad absorption features, we could be preferentially picking components with many narrow components that contribute to the total column density. We explore this possible selection effect further in the next section. Second, that the ‘no-low’ absorbers are the least common in galaxy halos is not surprising. This type tends to consist of lower O VI column density absorbers with broad line widths. Thus, its signal can easily be drowned out by the relatively stronger signals from ‘broad’ and ‘narrow’ matched components along the same lines of sight. The effect is similar to that which is pointed out by Zheng et al. (2015), in which they report the Milky Way CGM is ‘half-hidden’ by strong absorption from the ISM at $-100 \text{ km s}^{-1} < v_{\text{LSR}} < 100 \text{ km s}^{-1}$. We explore this effect further in Section 3.3.4.

3.3.2. Comparison between CGM and IGM O VI Absorption

There is extensive literature on the incidence of O VI gas along extragalactic sightlines and its association with galaxies and large-scale structures (e.g. Tripp et al. 2008; Wakker & Savage 2009; Prochaska et al. 2011b; Stocke et al. 2013; Savage et al. 2014). These ‘intervening’ O VI absorbers found along blindly-selected QSO sightlines have lower column densities ($\log N_{\text{OVI}} \approx 13.8$; Danforth et al. 2016) than the O VI gas seen in COS-Halos ($\log N_{\text{OVI}} \approx 14.8$). Statistically, the majority of the blindly-selected intervening O VI absorbers must occur far from L^* galaxies (Prochaska et al. 2011b), either around lower mass galaxies or in the IGM itself. One may consider, therefore, whether this gas constitutes a qualitatively different population with a unique physical origin.

Toward this end, we show a comparison of the distributions of Doppler b parameters from two studies of the low-redshift ($z < 0.9$) IGM (Savage et al. 2014; Danforth et al. 2016) with that of COS-Halos in Figure 7. Throughout this section, we will refer to Danforth et al. (2016) as D16 (crosshatched yellow histogram) and Savage et al. (2014) as S14 (crosshatched red histogram). All three studies detect O VI in HST/COS G130M or G160M spectra, and therefore have similar spectral resolution. The COS-Halos data (gray histogram) show a significantly larger fraction of broad O VI components, with a mean value of the Doppler b parameter of 55 km s^{-1} . Approximately 60% of the COS-Halos O VI line profiles have $b > 35 \text{ km s}^{-1}$, are symmetric, and have little internal structure, despite often aligning well with the more highly-structured low-ionization state absorption. Furthermore, both S14 and D16 find more narrow O VI lines than COS-Halos. A two-sided KS test between COS-Halos, S14, and D16, respectively, yields probabilities of the null hypothesis of 0.00041 and 0.0018. These differences between the samples could occur if COS-Halos

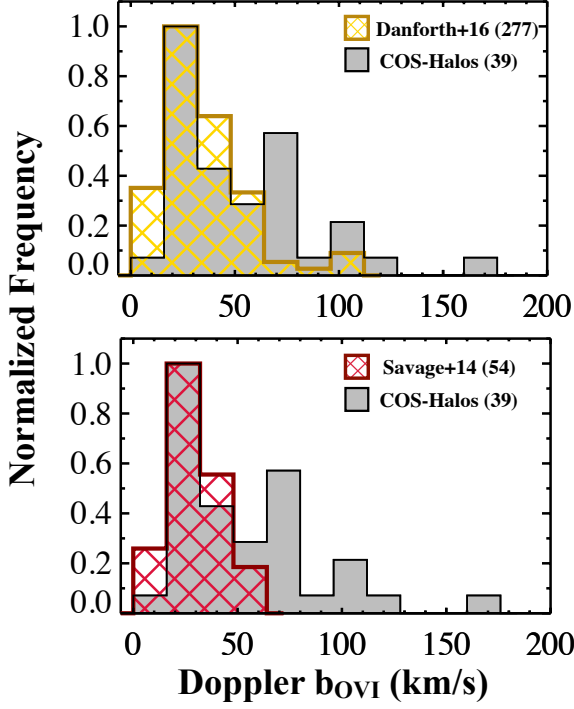


Figure 7. Distribution of the Doppler b parameter values for the 39 O VI components in the CGM of COS-Halos SF galaxies (gray histogram) compared to those of the low- z IGM absorbers studied in Danforth et al. (2016; D16, crosshatched yellow histogram, top panel) and Savage et al. (2014; S14, crosshatched red histogram, bottom panel). The histograms have been normalized such that the peak of each distribution is 1. The D16 distribution includes b parameters from 277 O VI components with a mean b parameter of 35 km s^{-1} while the S14 distribution includes 54 O VI absorber components that are well-aligned with H I, having a mean b -value of 30 km s^{-1} . In contrast, the mean of the COS-Halos O VI linewidths is 55 km s^{-1} .

O VI profiles consist of many blended components, such that narrow components are increasingly difficult to recognize. Or, they may indicate a physically distinct origin for CGM and IGM O VI.

The study by D16 includes HST/COS data of 82 UV-bright QSOs containing 280 O VI systems with $0.1 < z < 0.74$ (277 O VI $\lambda 1031 \text{ \AA}$ components shown; crosshatched yellow histogram). The mean of O VI b -parameters included in D16 is 35 km s^{-1} , with a low fraction of absorbers exhibiting values $> 60 \text{ km s}^{-1}$. Similarly, S14 find a mean value of b for O VI to be 29 km s^{-1} in 14 high S/N QSO spectra taken with COS (crosshatched red histogram). Although not shown on Figure 7, we also note that Muzahid et al. (2012) find a mean value of b for high- z ($1.9 < z < 3.1$) IGM O VI absorbers to be 28 km s^{-1} , and using higher resolution VLT UVES data. Using STIS E140M data, Tripp et al. (2008) find a mean O VI b -value of 27 km s^{-1} for 77 intervening absorbers at $z < 0.5$, with only 2 out of 77 O VI components with $b > 60 \text{ km s}^{-1}$ (see their Figure 13).

We caution that such comparisons of fitted absorption-line widths in spectra having different S/N and spectral resolution are subject to significant systematics. Our direct comparison between studies using COS spectra in Figure 7 eliminates the second source of bias, but the

mismatch between the S/N of the various studies could impact the b parameter distributions. The S/N of the COS-Halos data considered here is considerably lower (~ 10) than both D16 (S/N = 15 - 78) and S14 (S/N = 16 - 155). It is therefore possible higher quality spectra would reveal that weaker, narrower components comprise the very broad O VI we find in our data. Nonetheless, we find it unlikely that the difference in S/N is driving the difference between b -value distributions of the inner CGM and general IGM. In particular, a direct comparison between the Si III b -values included in the D16 study and those of COS-Halos give very good agreement: 25 km s^{-1} vs. 22 km s^{-1} respectively, even though Si III would be subject to the same systematics as O VI. Thus, despite the above caveats, we conclude that *very broad O VI absorption is an important characteristic of the CGM of star-forming L^* galaxies.*

3.3.3. Physical Insights from O VI Absorption Line Widths

In principle, the absorption line widths, quantified by the Doppler b parameter, encode physical information about the absorption. For example, one can place an upper limit on the gas temperature, assuming thermal line broadening, using the relation:

$$b_{\text{th}} = \left(\frac{2kT}{m} \right)^{\frac{1}{2}}. \quad (1)$$

Here, b_{th} is the thermal Doppler b parameter, k is the Boltzmann constant, T is the gas temperature, and m is the atomic mass. The typical velocity dispersions of the absorption components are small for the low-ionization state gas, with typical Doppler b values ranging from 5 km s^{-1} to 20 km s^{-1} . This range of b values implies the low-ion lines are marginally resolved or unresolved, and trace gas temperatures $\lesssim 10^5 \text{ K}$, consistent with a plasma photoionized by an incident radiation field. The Doppler b values of the O VI absorption lines are systematically higher for absorption components centered at the same redshift. This discrepancy in absorption line widths may indicate that O VI traces gas with a higher temperature, limited to $T \lesssim 10^{6.5} \text{ K}$. On the other hand, it may require that turbulence is dynamically significant for O VI in galaxy halos (see Faerman et al. 2016, for a detailed discussion), or that O VI spans a significantly larger fraction of a complex halo velocity field than the low-ion absorption lines (Stern et al. 2016).

We can roughly quantify the non-thermal component of the line width under the assumption of a characteristic temperature for O VI-bearing gas, where:

$$b^2 = b_{\text{th}}^2 + b_{\text{nt}}^2. \quad (2)$$

We proceed under the caveat noted previously regarding the possible blending of narrow components with velocity offsets $< 10 \text{ km s}^{-1}$ that can contribute significantly to the measured line widths. The measured line widths are also impacted by instrumental broadening, though we have tried to account for this as well as possible in our Voigt profile fitting procedure. As such, the non-thermal values reported here should be considered upper limits. Photoionization equilibrium models for optically thin gas give an equilibrium gas temperature, $T_{\text{PIE}} \approx 10^{4.5} \text{ K}$ (e.g. Ferland et al. 2013). Collisional ionization

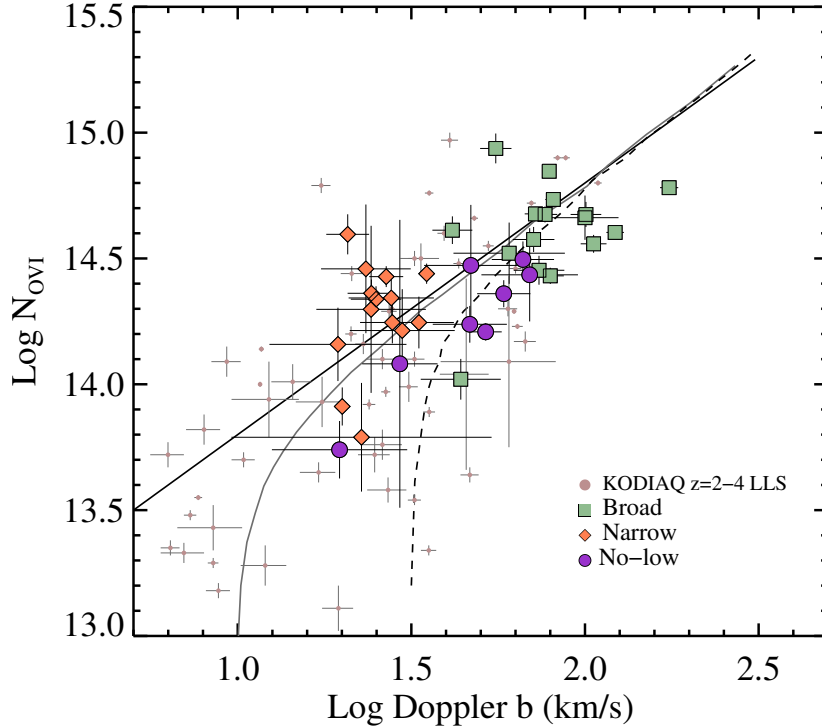


Figure 8. O VI column density versus Doppler b -parameters for the individual components colored by type: green is ‘broad’ type; orange is ‘narrow’ type; and purple is ‘no-low’ type. For comparison, we show the ‘robust’ estimates of the same parameters taken from the KODIAQ sample of $z=2-4$ Lyman limit systems as small light pink data points (Lehner et al. 2014). Their data were obtained with Keck/HIRES. The two curves show the expectations of $N-b$ behavior for radiatively cooling, collisionally-ionized gas for two temperatures, $T_{\text{OVI}} = 10^5$ K (black-dashed) and $T_{\text{OVI}} = 10^6$ K (solid gray) (Heckman et al. 2002). The curves are calculated assuming that the cooling flow velocity is equivalent to the b -value. The solid black straight line shows the effect of blending multiple narrow components with 0 km s^{-1} velocity offsets.

equilibrium models give $T_{\text{CIE}} \approx 10^{5.4}$ K where the abundance of O VI peaks (e.g. Gnat & Sternberg 2007; Oppenheimer & Schaye 2013b). Thus, the expected line widths of O VI in each case due to only thermal broadening are 6.4 km s^{-1} and 16.2 km s^{-1} , respectively. Both values are significantly lower than the majority of our measured b values for O VI. The average non-thermal contribution to the O VI line widths is $\sim 40 - 50 \text{ km s}^{-1}$. We note for Si III at $T_{\text{PIE}} = 10^{4.3}$ K, the expected line width due to thermal broadening alone is 3.4 km s^{-1} . Thus, the non-thermal contribution to the Si III line widths is limited to be $\lesssim 20 \text{ km s}^{-1}$.

Heckman et al. (2002) analyzed the relationship between O VI column density and absorption-line width for a wide range of physically diverse environments, incorporating measurements from the Milky Way HVCs, Magellanic Clouds, starburst galaxies, and the IGM. They found a relationship consistent with that predicted theoretically for a radiatively cooling flow of hot gas as it passes through the coronal temperature regime (Edgar & Chevalier 1986), shown as the dashed and solid gray lines here in our Figure 8. Wakker et al. (2012) describe in detail the radiative cooling flow model first proposed by Shapiro & Moore (1976) and later developed by Edgar & Chevalier (1986); Shapiro & Benjamin (1991); Benjamin (1994). This model allows gas to cool via collisions as it moves at a constant speed, and predicts the relation shown in Figure 8. Heckman and others (e.g. Bordoloi et al. 2016) have argued that this relationship, which spans orders of magnitude in column density, indicates

a generic origin of O VI in collisionally-ionized gas. As we discuss in Section 4, the authors note that radiatively cooling gas behind fast shocks is not the only physical model that can lead to the relationship between N_{OVI} and b (see also: Oppenheimer & Davé 2009). For example, turbulent mixing can give rise to such a relation since the inflow rate of mass is explicitly tied to the cooling rate in these models (e.g. Kwak et al. 2011).

In the 14 years following the result first shown by Heckman et al. (2002), there have been many others to investigate this correlation (or in some cases, its absence) extending it to stronger starbursting galaxies (Grimes et al. 2009), many more $z < 0.5$ intervening IGM absorbers (Tripp et al. 2008), $z = 2-4$ Lyman limit systems (Lehner et al. 2014), and incorporating modern measurements for the CGM and IGM (including COS-Halos; Bordoloi et al. 2016). We now explore this trend seen in the COS-Halos O VI absorbers in Figure 8, as a function of their kinematic subtype. We show the high- z LLS absorbers included in the KODIAQ sample (Lehner et al. 2014) for reference.

The first thing to notice about the data plotted in Figure 8 is that ‘narrow’ and ‘broad’ type O VI absorbers separate nicely on the b parameter axis. Of course, this is by design (see Section 3.3.1). Furthermore, each kinematic subtype traces a distinct region of the parameter space, with one or two exceptions. This facet of the figure is not explicitly by design, though selection effects may be playing some role in this separation. Second, it appears as though the O VI absorbers indeed

follow the trends delineated by the cooling flow curves. A Spearman-Rho test on the full sample indicates a 3.5 sigma correlation in the N_{OVI} vs. b parameter space, with a rank coefficient of 0.70. The ‘no-low’ type absorbers trace the lower edge of the N- b correlation seen in the data.

Now, we consider the above results in the context of the Heckman model. The solid black line shows the effect of blending multiple components with negligible velocity offsets, which, at the O VI column densities probed by COS-Halos, is nearly indistinguishable from the gray line, which marks gas radiatively cooling at $T_{\text{OVI}} = 10^6$ K. For increasing velocity offsets of the narrow, unresolved components, this solid black line moves down and to the right (see Heckman et al. 2002) and becomes even more consistent with the Heckman model predictions. For this reason, we cannot consider a priori the observed correlation to be a smoking gun for collisional ionization.

If component blending is indeed dominating the trend seen in Figure 8, we may expect to see such a correlation for the low-ionization state absorption components that are matched to the O VI components. There is no such correlation for *any* of the low or intermediate-ions, neither for only the matched components nor all low-ion components regardless of their O VI correspondence. Thus, we find it unlikely that the N- b correlation in Figure 8 is due to blending alone.

Finally, we point out that the ‘narrow’ type absorbers (orange diamonds) are actually inconsistent with the Heckman models to a significant degree. At the line-widths tracked by the ‘narrow’ lines, cooling flow models tracing 10^{5-6} K gas predict N_{OVI} values $< 10^{14} \text{ cm}^{-2}$, while 87% (13/15) of ‘narrow’ absorbers show N_{OVI} in excess of this value. Considered alone, ‘narrow’ type O VI absorbers do not exhibit any correlation between their column densities and line-widths. The ‘no-low’ absorbers (purple circles) are most consistent with the Heckman models, lie below the blending line, and track a rather tight, 2.5σ correlation between their column densities and line widths (the Spearman-Rho coefficient > 0.70), despite having only 8 data points. There are several other additional factors (some explored below) including broad associated H I and a complete lack of low-ionization state gas that make it likely this ‘no-low’ kinematic subtype represents gas cooling via collisional ionization. The ‘broad’ absorbers (green squares) alone only track a 1.6σ correlation as indicated by a Spearman-Rho test, and exhibit a considerable degree of scatter. Furthermore, as previously mentioned, this type of absorber is most prone to blending effects.

3.3.4. Correlating Kinematics with Galaxy Properties

The primary benefit of relying upon the COS-Halos dataset is the well-characterized host galaxy sample (Werk et al. 2012), and the resulting opportunity to relate the properties of the gas 10–150 kpc from a galaxy to the galaxy stellar and halo masses and global star-formation rates (SFRs). Toward this end, Figure 9 shows the difference between the galaxy systemic redshift (the assumed ‘rest’ frame) and the velocity centroids of the O VI components (Δv_{sys}) on the y-axis, as a function of the galaxy halo mass, determined by abundance matching (Werk et al. 2012; Tumlinson et al. 2013). To determine the ‘halo’ masses, as previously described by (Werk

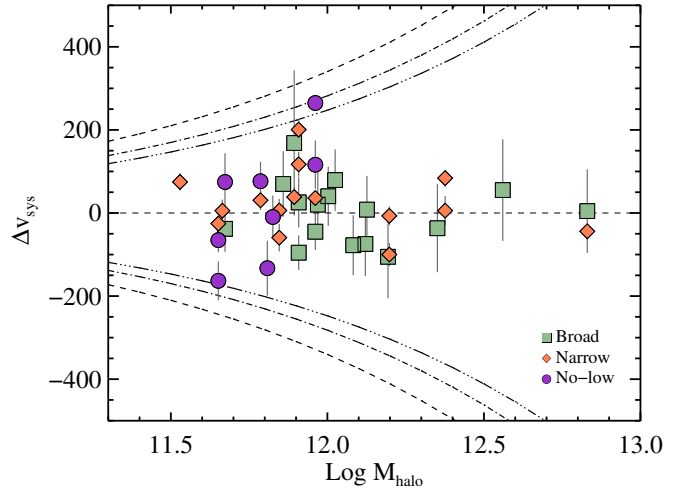


Figure 9. The difference between the galaxy systemic redshift (the assumed ‘rest’ frame) and the velocity centroids of the 39 O VI components in the 24 star-forming COS-Halos galaxy sub-sample addressed in this work, as a function of the galaxy halo mass, determined by abundance matching (Werk et al. 2012; Tumlinson et al. 2013). As in previous figures, the data points are colored by kinematic subtype: green squares indicate ‘broad’ type O VI absorption; orange diamonds show ‘narrow’ type absorption; and purple circles mark the ‘no-low’ type absorption. The vertical gray lines track the line-widths of the components, with a total length given by $\pm b_{\text{Doppler}}$. From the inside moving outward, the curves trace the halo escape velocities from 50, 100, and 150 kpc, respectively.

et al. 2014), at a galaxy stellar mass given by k_{correct} (Blanton et al. 2003) from the SDSS *ugriz* photometry, we interpolate along the halo abundance matching relation of Moster et al. (2010).

It is immediately apparent from Figure 9 that the broad O VI absorbers with no corresponding low-ionization state gas (‘no-low’; purple circles) are absent in galaxies with $\log M_{\text{halo}} > 12.0$. A two-sample KS test on the ‘no-low’ M_{halo} distribution vs that of the ‘broad’ and ‘narrow’ types indicates this absence is statistically significant at the 3σ level with a Kolmogorov-Smirnov statistic of 0.6. Furthermore, these kinematic subtypes were selected without regard to galaxy properties, and there is no plausible selection effect that could account for the absence of O VI absorbers in the star-forming galaxies with more massive halos. We do note that we are likely to miss a significant fraction of ‘no-low’ absorbers potentially washed out by strong ‘broad’ and ‘narrow’ absorbers along the same sightline, however that will bias the impact parameter distribution of the kinematic subtypes, as we discuss later in this section. COS-Halos evenly samples the full range of halo masses in impact parameter space for the 24 galaxies considered.

The distribution of Δv_{sys} compared to the halo escape velocities is the other striking feature of Figure 9. For both ‘broad’ and ‘narrow’ type absorbers coincident with low-ionization state gas, the Δv values are rather tightly concentrated around 0 km s^{-1} as compared to the allowed range of Δv for bound gas especially for $\log M_{\text{halo}} > 12$. In contrast, the ‘no-low’ type absorbers occupy the full range of allowed Δv for their given range of M_{halo} . As we will discuss in Section 6, the virial temperature for $11.5 < \log M_{\text{halo}} < 12.0$ is $10^{5.3-5.5} \text{ K}$, *exactly* the temperature at which the O VI gas fraction peaks in col-

lisional ionization models, both in and out of equilibrium (e.g. Oppenheimer et al. 2016, see their Equation 1). We will argue that the abrupt truncation of the halo mass distribution at $\log M_{\text{halo}} < 12.0$, and the statistically significant correlation between $\log N_{\text{O VI}}$ and b values for the ‘no-low’ type absorbers are strong pieces of evidence that this kinematic subtype is tracing halo gas at $T \approx T_{\text{vir}}$, cooling via collisions.

We turn now to the top panel of Figure 10, which shows $N_{\text{O VI}}$ as a function of impact parameter, R , with data colored by kinematic subtype. The global COS-Halos trend for star-forming galaxies, which uses the total integrated $N_{\text{O VI}}$ within $\pm 300 \text{ km s}^{-1}$ of galaxy systemic, is shown by the dashed black line with 1σ uncertainty marked by the gray shaded region for reference. As discussed previously, the ‘no-low’ type absorbers are found only at $R > 50 \text{ kpc}$, possibly due to selection effects that cause the low-column density broad absorption lines to be blended with ‘narrow’ and ‘broad’ type absorbers along the longer total path lengths probed at lower impact parameters. Additionally, we point out that the ‘broad’ type O VI absorbers with matched low-ion counterparts are setting the global COS-Halos trend between $N_{\text{O VI}}$ and R . This is unsurprising given the previous observation that these absorbers dominate the total column density of the SF galaxies. Yet it is significant; Figure 10 leads us to conclude that ‘broad’ type absorbers drive the global correlations between O VI and galaxy properties.

Perhaps the most perplexing trend apparent in the full COS-Halos sample is the correlation between the global galaxy SFR and the total integrated O VI column density (Tumlinson et al. 2011). Particularly significant is the strong presence of O VI absorption around star-forming galaxies and its rarity around galaxies with no detectable level of star-formation. This dichotomy may imply that the material bearing O VI is somehow transformed or lost from the CGM once the galaxy’s star formation quenches (but see: Oppenheimer et al. 2016). For the star-forming galaxies in consideration here, galaxy SFR and $N_{\text{O VI}}$ are not significantly correlated (40% chance a correlation is not present), though we do note that the significance of this correlation increases to 3σ (0.1% chance a correlation is not present) when we consider the upper limits to the SFR and $N_{\text{O VI}}$ implied by the spectroscopic observations of the 16 passive galaxies in the COS-Halos sample.

In Section 4, we will explore the evidence for (and rather dramatic implications of) O VI being produced in part by ionizing radiation either indirectly or directly due to the galaxy’s ongoing SFR. If this were true, we might expect its strength to correlate directly with SFR/R^2 , which is explored in the bottom panel of Figure 10. Additionally, we note that other phenomena, such as starburst driven winds, may also result in such a correlation. On this figure, we show the 2.7σ correlation¹³ for the total integrated $N_{\text{O VI}}$ as a function of SFR/R^2 as the dashed black line with the 1σ errors enclosed in the gray shaded area. The power law fit with 1σ errors is:

$$N_{\text{O VI}} [\text{cm}^{-2}] = 10^{15.1 \pm 0.17} \left(\frac{\text{SFR}}{R^2} \right)^{0.16 \pm 0.05} \quad (3)$$

¹³ More specifically, there is a 0.8% chance a correlation is not present; according to a Kendall-Tau test including measurement errors and censoring by lower limits.

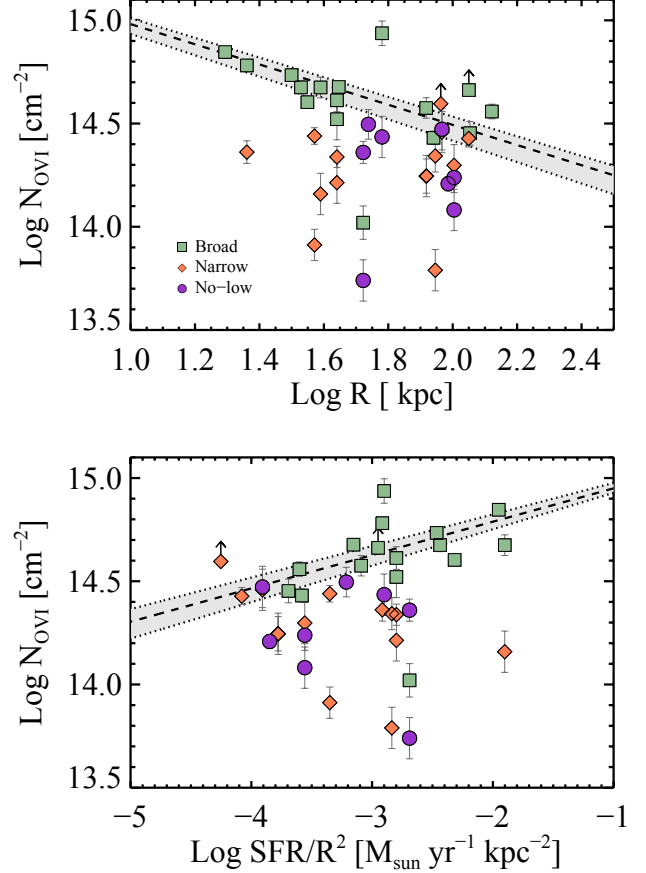


Figure 10. Top: $\log N_{\text{O VI}}$ as a function of impact parameter, R , for the individual O VI components colored by type where green squares indicate ‘broad’ type O VI absorption; orange diamonds show ‘narrow’ type absorption; and purple circles mark the ‘no-low’ type absorption. The 2.9σ correlation between the total line of sight AODM column densities and impact parameter is shown as a dashed line with 1σ uncertainty marked by the gray shaded area. The ‘broad’ type absorbers dominate and define this trend, while the other two types exhibit no correlation between $\log N_{\text{O VI}}$ and R . Furthermore, the ‘no-low’ type absorbers (purple circles) lie at impact parameters $R > 50 \text{ kpc}$, while the other two types span the full range of impact parameters. Bottom: Similar to the top plot, but now the x-axis shows the galaxy SFR, scaled inversely by the impact parameter squared. The 2.7σ correlation for the total $N_{\text{O VI}}$ for each galaxy halo (i.e. not by component) is shown in light gray. The ‘broad’ type absorption in each galaxy halo is driving the overall correlation between $\log N_{\text{O VI}}$ and SFR/R^2 . The other two types are not correlated at all with SFR/R^2 (or SFR).

where SFR is in $M_{\odot} \text{ yr}^{-1}$ and impact parameter, R , is in kpc. We note that this correlation is driven primarily by the decrease in $N_{\text{O VI}}$ with impact parameter, and could just as easily represent a gas surface density gradient in the galaxy halo. Furthermore, neither the ‘narrow’ nor ‘no-low’ absorber column densities are correlated with SFR/R^2 .

4. ANALYSIS OF IONIZATION PROCESSES

We now explore the various ionization processes that may produce a highly ionized plasma bearing O VI. We then test whether these scenarios are consistent with the observed column densities (or limits, in many cases) of other intermediate and high-ions (i.e. Si IV, N V) and their kinematics. For this analysis we primarily focus on the column density ratios of N V/O VI for 38/39 O VI components detected in COS spectra that also cover the

N V doublet at $\lambda\lambda$ 1238.8, 1242.8 Å. For all but three of these components, the column density ratios are upper limits due to the non-detection of N V, and should be interpreted as such.

It is entirely possible that N V does not trace the same gas phase as O VI. The two ionization potential energies, ~ 98 eV and ~ 138 eV, respectively, differ by 40 eV. For example, one of the IGM absorbers analyzed by Tumlinson et al. (2005) along the QSO line of sight to PG 1211+143 shows broad O VI consistent with collisionally-ionized, warm gas, and weak, but narrow N V, consistent with photoionization (see also: Savage et al. 2011). In contrast, Fox et al. (2009) in their analysis of N V detected in damped Ly α systems find a detection rate of N V to be only 13%, and to have roughly equal contributions from broad and narrow components. For the N V components in our sample, all have b values ≈ 25 km s $^{-1}$. However, we caution that the N V is fairly weak when detected, and the S/N does not allow for very robust profile fits in the few cases of detections. Of the three O VI components that match up with N V components, one is in a ‘narrow’ kinematic type absorber, with $b_{\text{OVI}} = 23$ km s $^{-1}$. The other two are found in ‘broad type’ O VI absorbers with $b_{\text{OVI}} = 72$ and 79 km s $^{-1}$.

For cross comparison with the O VI components, we give their QSO and galaxy identifiers, along with their velocity centroids, $\log N_{\text{NV}}/N_{\text{OVI}}$, and kinematic subtype:

1. J1016+4706_359.16: $v_{\text{cen}} = -68$ km s $^{-1}$;
 $\log N_{\text{NV}}/N_{\text{OVI}} = -0.78^{14}$, ‘broad’ type O VI
2. J1241+5721_199.6: $v_{\text{cen}} = 65$ km s $^{-1}$;
 $\log N_{\text{NV}}/N_{\text{OVI}} = -1.28$, ‘broad’ type O VI
3. J1241+5721_208.27: $v_{\text{cen}} = 33$ km s $^{-1}$;
 $\log N_{\text{NV}}/N_{\text{OVI}} = -0.83$, ‘narrow’ type O VI

We suggest inspecting Figure 4 on the corresponding panels at the listed velocities. It is not evident by the kinematics that N V, when detected, traces the same gas-phase as O VI. The component structure of N V in some cases appears to match that of the low-ionization state gas, and may be more highly structured than the O VI. The S/N of the data make it difficult to draw a more robust conclusion from examining the few detections of N V. We pointed out in Figure 3 that single-density photoionization models based on low-ions under-predict the column density of Si IV; the same can be said for the three cases of detected N V absorption. We do note that the kinematics of intermediate ions such as C IV and Si IV often bear a higher degree of similarity to low-ions than to high-ions (e.g. Burchett et al. 2015). It is not a given that O VI would exist in this same gas phase as intermediate ions, especially in the cases of ‘broad’ and ‘no-low’ types. Indeed, none of the ‘no-low’ absorbers have intermediate ion detections. We remain agnostic for now, but must proceed with caution.

N V is not detected in *any* gas phase in 35/38 components considered. Thus, its upper limit can be used in comparison against O VI in *both* photoionization and

collisional ionization models for a single-phase gas. Indeed, we will see that the constraints imposed by the non-detection of N V in both photoionized gas and collisionally-ionized gas are meaningful. Furthermore, there are two models that attempt to explain *all* ion detections in a self-consistent fashion, namely photoionization models that incorporate steep density gradients in the absorbing gas (e.g. Stern et al. 2016). In those cases, a comparison of the column densities of Si IV, N V, and O VI is instructive.

Savage et al. (2014) have recently reviewed some of the processes other than photoionization that produce O VI, which include: CIE and non-CIE non-dynamical radiative cooling models (Edgar & Chevalier 1986; Gnat & Sternberg 2007), dynamical radiative cooling models (Shapiro & Benjamin 1991; Wakker et al. 2012), shock ionization models (Dopita & Sutherland 1996), conductive interfaces between cool clouds and a hot medium (Borkowski et al. 1990), and non-equilibrium turbulent mixing layers (Begelman & Fabian 1990; Slavin et al. 1993; Kwak & Shelton 2010; Kwak et al. 2011). Many of these processes have been invoked for the highly ionized component associated to Galactic HVCs (Savage et al. 2000; Fox et al. 2004). Additionally, it is possible to produce O VI via photoionization, with the gas very highly ionized by the EUVB, or by radiation from the galaxy in addition to the EUVB that includes soft x-rays (Cantalupo 2010; Vasiliev et al. 2015). For photoionization in equilibrium we use the Cloudy software package (v13.03; Ferland et al. 2013) and for non-equilibrium photoionization modeling and collisional ionization calculations, both in and out of equilibrium, we use the tables of Oppenheimer & Schaye (2013b).

4.1. Photoionization by the Extragalactic UV-Background

We now consider the photoionization of an infinite homogeneous slab of optically-thin gas illuminated by an incident extragalactic ultraviolet background (EUVB) radiation field. This type of photoionization modeling successfully reproduces the observations of the low-ionization state ions (i.e. the Si III-bearing gas; see Werk et al. 2014), and we explore here whether this simple model can be applied to the more highly ionized gas, though at lower gas densities.

Figure 11 shows $\log N_{\text{NV}}/N_{\text{OVI}}$ as a function of hydrogen volume density for a simple Cloudy-based model with the EUVB radiation field of Haardt & Madau (2001). The pink line tracks a fiducial model of optically thin $Z = Z_{\odot}$ gas where $\log N_{\text{HI}} = 15$ cm $^{-2}$, since most of the HI seen in COS-Halos is likely associated with the low-ions. Along the y-axis we show the distribution of $\log N_{\text{NV}}/N_{\text{OVI}}$ for the 38 components, 35 of which are upper limits. The histogram is labeled according to the number of components in each bin. We note that all three kinematic subtypes show very similar distributions of their upper limits to $\log N_{\text{NV}}/N_{\text{OVI}}$. Therefore it is not instructive to color the histogram by the O VI kinematic component type (though Figure 12 shows the actual ratios colored by kinematic type for reference).

The EUVB we use has a total photon flux $\Phi_{\text{HMO1}} = 4.8 \times 10^4$ cm $^{-2}$ s $^{-1}$ (Haardt & Madau 2001) for a series of assumed dimensionless ionization parameters $\log U \equiv \Phi/n_{\text{H}}c$, which are shown and labeled along the pink line.

¹⁴ This absorber has no spectral coverage of Si IV so it is not included in Figure 12.

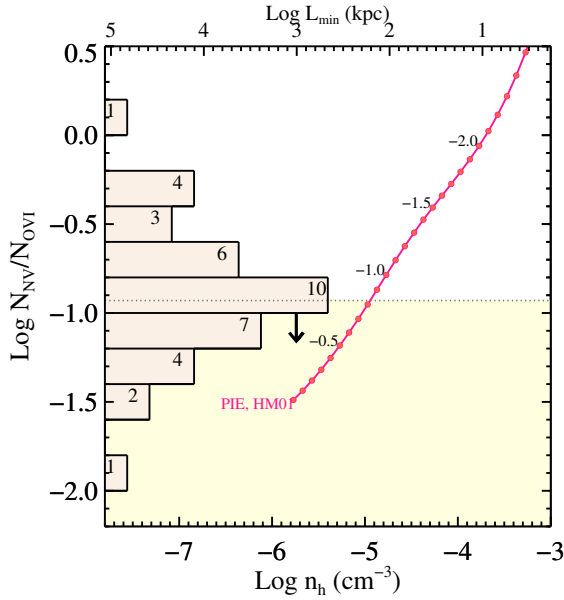


Figure 11. Column density ratios N_V / N_{OVI} as a function of hydrogen volume density for a simple Cloudy-based model shown in pink in which a single-density slab of $Z = Z_\odot$, and $\log N_{HI} = 15 \text{ cm}^{-2}$ gas is photoionized by a HM2001 EUVB. The corresponding minimum path lengths are shown on the top x-axis. We show a histogram of the observed ratios for the individual components on the y-axis for reference, noting with the downward-facing arrow that the vast majority of these column density ratios are upper limits due to the non-detection of N V for the majority of the O VI components. The pink model curve traces a series of points that correspond to the dimensionless gas ionization parameter, $\log U$, and we label several values along the curve. The yellow-shaded area highlights the typical COS-Halos measured column density ratios of $N_V / N_{OVI} < -0.93$. Gas ionization parameters with $\log U > -0.8$ are allowed by the majority of the data.

The range of $\log N_V / N_{OVI}$ allowed by the majority of the data is shaded light yellow. The observations require $\log U \gtrsim -1$ to achieve crude consistency with the data. Such high $\log U$ values are characteristic of gas close to quasars and would require a very low gas density for our COS-Halos systems. Regarding Φ , the average EUVB is well bounded to have $\log \Gamma_{HI} \sim 13$ (Davé et al. 1999; Davé & Tripp 2001) and cannot conceivably provide a high U value on its own, i.e. for gas with a modest density, $n_H > 10^{-5} \text{ cm}^{-3}$.

Figure 11 also shows a minimum path length for this highly-ionized gas on the top y-axis, computed as N_O / n_O , and given in kpc. For example, a value of $\log U > -1.0$ would require $n_H \lesssim 10^{-5} \text{ cm}^{-3}$ or $n_O < 10^{-8.3} \text{ cm}^{-3}$, for a solar metallicity gas. This gas volume density implies a length scale $L \sim N_{OVI} / n_O > 20 \text{ kpc}$ based on N_{OVI} alone. We conservatively convert N_{OVI} to N_O assuming the maximum fraction of gas in O VI allowed by the photoionization models (or any model, because of the cooling function), 0.25, implying an additional factor of ~ 4 in size. Gas metallicities below solar would increase this minimum length scale, to e.g. 1 Mpc for $Z/Z_\odot = 0.1$. This conservative length-scale thus likely exceeds the extent of the dark matter halos hosting L^* galaxies. Furthermore, these constant density models would be severely challenged to yield the observed coherence in velocities (e.g. Figure 5), especially for the ‘narrow’ kinematic types. We conclude that *the standard EUVB, constant-density photoionization models are*

ruled out altogether for the OVI-bearing gas around L^ star-forming galaxies.*

Figure 12 presents the observed ionic ratios $\text{Si IV} / \text{O VI}$ versus N_V / N_{OVI} for 28 individual matched O VI components along sightlines that cover both N V and Si IV. The data points are colored by kinematic type, though each kinematic type traces roughly the same range of N_V / N_{OVI} and $\text{Si IV} / \text{O VI}$ especially given that the majority of these points are upper limits on both axes. Non-detections in N V give a characteristic upper limit (left-facing arrows) $\log(N_V / N_{OVI}) \lesssim -0.9$, set by the S/N of the COS spectra and the measured N_{OVI} values. The ratio of $\text{Si IV} / \text{O VI}$ tends to lie around -1 or lower, in the cases of upper limits. We note that the majority of the data points shown in Figure 12 should occupy a region of parameter space to the left of and/or below the locus of points. The lines on Figure 12 present the column density ratios predicted by several photoionization models that we will explore in detail. For reference, one of these models (light gray line, with black circles) is the simple Cloudy photoionization equilibrium model already ruled out, above.

We use the models for photoionization out of equilibrium (PINE) of Oppenheimer & Schaye (2013b), which tracks the ionization states of a suite of the atoms most important for gas cooling and calculates the non-equilibrium cooling rates. They assume equilibrium initial conditions ($t = 0$) of $n_H = 10^{-4} \text{ cm}^{-3}$ and $T = 10^6 \text{ K}$. Within 1 Gyr the gas temperature drops below $T < 10^5 \text{ K}$. In the presence of efficient cooling, for the metal-enriched gases of the CGM (assumed to be $1/10 Z_\odot$), the observational diagnostics are altered somewhat from the equilibrium case. In Figure 12, the dotted black line shows the isobaric PINE model of Oppenheimer & Schaye (2013b) at $n_H T = 10 \text{ K cm}^{-3}$. The other PINE models (including the isochoric models) fall to the right of this curve. PINE alleviates some of the concern of the equilibrium case (PIE, gray line), in that the density does not need to be extremely low to match the data points with the highest allowable N_V / N_{OVI} . In isobaric PINE, the density increases when cooling at a constant pressure, which allows for lower U . Yet, PINE cannot explain the majority of the observed ratios (or limits), because like PIE, it over-predicts the ratio N_V / N_{OVI} .

4.2. Photoionization Models Including a Density Gradient in the Absorbing Cloud

Let us now consider a departure from typical photoionization models that assume a homogenous slab of gas with a constant density, and instead allow a density gradient that increases toward the center of the absorber. The low-ions will be located in the central compact, denser regions, while the high-ions will lie in the outer, lower-density gas. The specific location of the line of sight intercepting the cloud will affect the observed properties of the absorber.

Stern et al. (2016) explores such a phenomenological model in detail, presenting a universal density gradient (UDG) for cool clouds in the CGM that explains the gas column densities of the full suite of ions covered by COS-Halos, from Mg II to O VI. We show the expectation of $\log N_{\text{Si IV}} / N_{OVI}$ vs. $\log N_V / N_{OVI}$ for their model in Figure 12 as the blue dashed curve marked with triangles for values of the maximum $\log n_H$, or the maximum

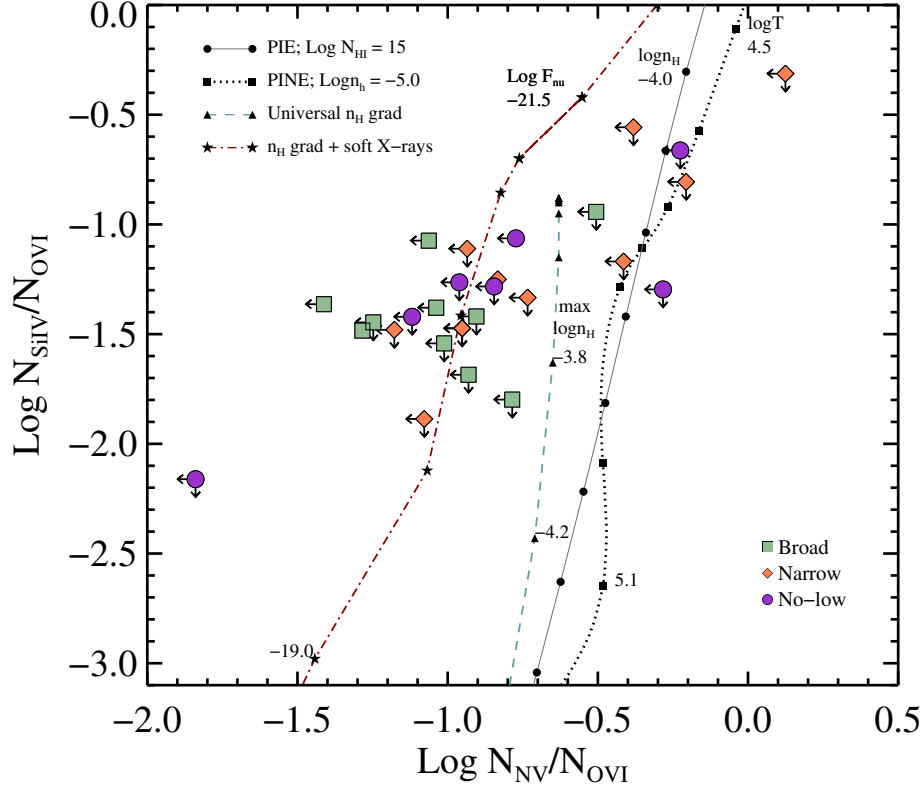


Figure 12. Ionic ratios, $\log N_{\text{NV}}/N_{\text{OVI}}$ versus $\log N_{\text{SiIV}}/N_{\text{OVI}}$, for the matched components. As in previous figures, green squares indicate ‘broad’ type O VI absorption; orange diamonds show ‘narrow’ type absorption; and purple circles mark the ‘no-low’ type absorption. We show the predictions of various photoionization models as curved lines, for reference. The light gray line with black circles on the upper right shows a single-density ‘slab’ photoionization model in thermal and ionization equilibrium (PIE), photoionized by an HM2001 EUVB, with $\log U$ ranging from -1.5 to -0.5 ($\log n_{\text{H}} < -4.0 \text{ cm}^{-3}$), and $\log N_{\text{HI}} = 15 \text{ cm}^{-2}$. PIE models with $\log N_{\text{HI}} < 17 \text{ cm}^{-2}$ lie to the right of the line shown, and are therefore less consistent with the data. We show a model of metal-enriched gas ($Z = Z_{\odot}$) photoionized by the EUVB cooling out of equilibrium (PINE) for the isobaric case of $n_{\text{H}}T = 50$ given by Oppenheimer & Schaye (2013b) as the dotted line curve marked by black squares. Isothermal models for lower metallicity and higher gas densities tend to lie to the right of the plotted curve. The filled squares on the PINE curve represent different temperatures ranging from $10^{4.5} < T < 10^{5.1}$, with the lowest temperature at the upper right. The red dashed-dot curve with black stars is a model developed by Cantalupo et al. (in prep) that assumes clouds with a steep density gradient that are photoionized by the EUVB and an extra blackbody component to the ionizing radiation with $T = 10^5 \text{ K}$. The stars on this curve correspond to different intensities of the extra component ranging from $\log 4\pi J_{\nu}$ at 10 Ryd of -22.0 (top right) to -19.0 (lower left). Finally, the blue dashed line with triangles shows the predictions of Stern et al. (2016) for the phenomenological universal density model in which small high-density clouds are hierarchically embedded in larger low-density clouds. The triangles mark values of the maximum $\log n_{\text{H}}$, which occurs in the cloud core. Where $\log n_{\text{H,max}} > -3.0$, the line ratios saturate.

density of the absorber along the line of sight. The typical length scales and densities predicted by the model have a range of approximately three orders of magnitude from the inner ‘cloud’ to the outer low-density outskirts. For example, the UDG model predicts O VI lives in the outermost layer of the cloud, characterized by a gas density of $\sim 2 \times 10^{-5} \text{ cm}^{-3}$, and path lengths $\sim 30 \text{ kpc}$. In contrast, Mg II is confined to the inner 49 pc and has a density of $\sim 6.5 \times 10^{-3} \text{ cm}^{-3}$ (Stern et al. 2016).

Figure 12 shows that $> 50\%$ of the upper limits to the $\log N_{\text{NV}}/N_{\text{OVI}}$ are inconsistent with the predictions of the UDG. The mean *upper limit* to $\log N_{\text{NV}}/N_{\text{OVI}}$ for the 38 components that cover N V is -0.9 , while the value predicted by the universal density model is typically ~ -0.8 for a large range of maximum gas densities. Figure 4 of Stern et al. shows that the UDG slightly over-predicts upper limits to N_{NV} , which is the

source of the discrepancy. As we noted in Section 2.2, the single-density photoionization models of COS-Halos data are broadly consistent with solar N/O ratios. However, it may be possible to further tune the UDG to include sub-solar N/O ratios (and still account for the observed N II and N III). Such an adjustment might be one avenue by which to bring the UDG into agreement with the constraints placed on $\log N_{\text{NV}}/N_{\text{OVI}}$ by the COS-Halos data.

One appealing facet of the UDG model is that it simultaneously explains the column densities of both low and intermediate ions very well, resolving the tension between Si IV and the low-ions that is present in single-density Cloudy models. Furthermore, the UDG implied length scales for Si IV are a modest $\sim 4 \text{ kpc}$, which would not necessitate large differences in the velocity structure of the Si IV absorption compared to the

Si III absorption (see Figure 4). Finally, the UDG brings the column density predictions for Si III and Si II into better agreement than found in single-density models. However, density gradients may be difficult to maintain for timescales greater than the sound-crossing time ($\sim 10^6$ years for 10^4 K gas) without continual shocking. Future studies addressing the physical origin of the UDG will have to discuss the formation and maintenance of the required gradient, without significant contribution from collisional ionization in the wakes of shocked material.

4.3. Additional Sources of Radiation

Metal-line diagnostics, such as the ratio of N V to O VI, depend critically upon the spectral shape and strength of the ionizing radiation. The EUVB is calculated assuming galaxy escape fractions, intrinsic spectral slopes of QSOs, and extrapolations of luminosity functions, all of which are uncertain (Haardt & Madau 2001, 2012). For example, at the energy required to ionize O V to O VI (114 eV), the uncertainty in the shape and intensity of the EUVB can contribute up to an order of magnitude uncertainty in the derived ionic abundances (Oppenheimer & Schaye 2013b). This is true also at the energy where N IV is ionized to N V (77 eV). By extension, the uncertainty of the contribution of ionizing radiation from the host galaxy can have a major impact on the metallic ion ratios. Moreover, hot gas is capable of producing significant additional ‘self-ionizing’ radiation (Gnat et al. 2010), which in turn depends on the mechanism of ionization in the hot gas. Here we explore the effect of adding additional sources of ionizing photons to the EUVB, which will change both the overall intensity and shape of the incident radiation field.

As the absorption we observe occurs within 160 kpc of a nearby galaxy, the EUVB may be supplemented or even exceeded by a local ionizing radiation field from sources within the galaxy. The simplest implementation of this idea is to scale the total ionizing flux, Φ_{tot} , with impact parameter ($\propto 1/R^2$), galaxy star formation rate ($\propto \text{SFR}$), and the escape fraction of ionizing photons ($\propto f_{\text{esc}}$). Moreover, there is some observational motivation for considering such a local ionizing radiation field given the correlation observed for ‘broad’ type absorbers between N_{OVI} and SFR/R^2 , as mentioned in Section 3.3.4. Such an increase in Φ_{tot} would ease the requirements for low gas density found in Werk et al. (2014), and the implied huge length scales discussed in Section 4.1 because $n_{\text{H}} \propto \Phi_{\text{tot}}/U$. Yet, the inclusion of only stellar radiation from a Starburst99 spectrum (Leitherer et al. 1999) will not provide the increase in $\log n_{\text{H}}$ required unless the SFRs are extreme. For example, if the galaxy SFR exceeds $50 M_{\odot} \text{ yr}^{-1}$ for sightlines with $R < 50$ kpc assuming $f_{\text{esc}} = 5\%$, the gas density will increase by two orders of magnitude. For reference, the average SFR for the COS-Halos star-forming galaxies is approximately $1 M_{\odot} \text{ yr}^{-1}$ and the average impact parameter is 72 kpc. We must therefore consider additional sources of ionizing radiation that are not included in the starburst99 galaxy SED (Leitherer et al. 1999).

In their investigation of how photoionization by local sources regulates gas cooling, Cantalupo (2010) use a galaxy SED that incorporates soft X-ray emission produced by mechanical energy released into the ISM during a starburst phase, from both supernovae and addi-

tional X-ray sources produced by star-formation. This SED is calibrated to reproduce the empirical relation between soft X-ray emission and SFR presented by Cerviño et al. (2002). Along with other ionizing radiation from the galaxy, some fraction of the soft X-rays escape into the CGM. Though less physically-motivated, the SED of Vasiliev et al. (2015) also shows an extra soft X-ray component. In this case, the authors simply sum together a PEGASE SED, an X-ray power-law spectrum, and an EUVB in a time-dependent radiation field to investigate how a local radiation field including X-rays impacts the ionization fraction of O VI. The break in their spectrum at 91 Å is due to the lack of data at higher energies in the PEGASE data rather than having a physical origin. Nonetheless, both the Cantalupo (2010) and Vasiliev et al. (2015) SEDs, when added to the EUVB, produce an excess of high-energy photons (> 8 Ryd) relative to those with energies between 4–8 Ryd. The latter are partially absorbed by the galaxy ISM, with He and dust being important sources of opacity.

In Figure 12, we show a toy model that includes an excess of radiation at energies > 50 eV as the red dashed-dot line with stars. For simplicity, we make the following assumptions (a more detailed model exploring a larger parameter range will be presented in Cantalupo et al., in prep.): (1) The SED of the ionizing radiation is a composite of a blackbody with $T=10^5$ K, absorbed intrinsically by a galaxy with $N_{\text{H}}=10^{20} \text{ cm}^{-2}$, and an EUVB at $z=0.2$; (2) The cloud is a plane parallel slab with total column of $N_{\text{H}}=10^{20} \text{ cm}^{-2}$, with an inwardly-increasing density distribution having an initial volume density, $\log n_{\text{H}_0} = -3.5$ with the scale factor $N_{\text{H}_0}=10^{19}$. This density profile obeys the relation: $n(r) = n_{\text{H}_0}(r_0) \times (1 + N_{\text{H}}/N_{\text{H}_0})^2 [\text{cm}^{-3}]$ and is less steep than the universal density gradient explored by Stern et al. (2016). The density decreases by a factor of ~ 100 toward the outer regions the cloud. The model, shown as the red dashed-dotted line in Figure 12, does well in reproducing the ionic ratios Si IV/O VI and N V/O VI and the total column densities for the majority of the absorbers¹⁵. Each star represents a unique value of the intensity of the extra blackbody SED component with values of $\log 4\pi J_{\nu}$ at 10 Ryd between -22.0 (top right) and $-19 \text{ ergs s}^{-1} \text{ cm}^{-2} \text{ Hz}^{-1}$ (lower left). The predictions of $\log N_{\text{OVI}}$ range from 13.52 to 15.1, coincident with the observed values.

The main utility for this toy model lies in constraining the intensity of the extra component in conjunction with the gas density (ionization parameter) required for photoionization to remain a viable model for the COS-Halos O VI absorbers: $\log 4\pi J_{\nu}$ at 10 Ryd $> -21.5 \text{ ergs s}^{-1} \text{ cm}^{-2} \text{ Hz}^{-1}$ for $\log n_{\text{H}} = -3.5 \text{ cm}^{-3}$. To first order, the required J_{ν} will scale with density. For reference, the EUVB produced by quasars and galaxies at $z \sim 0.2$ provides $\log 4\pi J_{\nu}$ at 10 Ryd = -23.7 for HM01 and -23.2 for HM12 (Haardt & Madau 2001, 2012). As we have seen, the EUVB is by itself orders of magnitude too weak to account for the observed ionization states of the CGM gas if photoionization is the dominant mechanism. The success of the Cantalupo model relies also on the density gradient, since Si IV is partially shielded by H I and

¹⁵ This model matches the low ionization state lines well, since the SED below ~ 10 Rydberg is unchanged.

tends to live in the denser part of the cloud with the other low-ions.

This model further necessitates that O VI reside in a cool, $<10^5$ K phase. The large path lengths implied by EUVB-only photoionization ($\gtrsim 100$ kpc) models are now mitigated by the increase in Φ , and on the order of $\sim 1\text{--}10$ kpc (see Section 4.1). In the COS-Halos dataset, O VI is often significantly broader than the low-ions, possibly indicating a temperature limit that is > 6 times as high as that for the low-ions. However, if large scale motions of the gas or turbulence contribute significantly to the line width, then these assumptions about temperature inferred from the line widths are incorrect. In general, for ‘narrow’ and ‘broad’ O VI kinematic subtypes, the gas kinematics are consistent with O VI arising in the same structure as the low-ions, since the offsets in the velocity centroids are typically ~ 20 km s $^{-1}$.

Using $\log 4\pi J_\nu \gtrsim -21.5$ ergs s $^{-1}$ cm $^{-2}$ Hz $^{-1}$, we may constrain the luminosity of the unknown sources the model requires at ~ 10 Ryd and compare with that of potential candidates for the emission. At distances > 10 kpc, this luminosity $\nu L_\nu > 10^{40}$ erg s $^{-1}$ at ~ 10 Ryd. Unfortunately, this emission energy, ≈ 0.13 keV, is outside of the classical bands of X-ray instruments (e.g. Chandra), and our own galaxy typically absorbs most of the extragalactic radiation at these energies. The main sources of radiation at these soft X-ray energies, excluding fluctuating AGN (e.g. Oppenheimer & Schaye 2013a) and possible contribution from X-ray binaries, are expected to be the hot ISM (heated by supernovae) and the so-called “supersoft X-ray sources (SSSs)” (Greiner 2000). Soft X-ray emission from the ISM is known to correlate with the galaxy SFR, and in all star forming galaxies there is at least one optically thin thermal emission component with an average temperature of $\langle kT \rangle = 0.24$ keV (e.g. Mineo et al. 2012). Although the derived intrinsic bolometric luminosity from this gas is consistent with our model requirements at $d > 10$ kpc, the luminosities are model dependent and require extrapolation to the lower energies. Additional sources of high-energy photons could arise from the SSSs. First identified more than two decades ago by the Einstein Observatory, these close binaries are characterized by significant emission in the $0.3\text{--}0.7$ keV band. Their SED resembles the tail of a blackbody with effective temperatures of a few $\times 10^5$ K (Greiner 2000). In the disks of ordinary star forming galaxies like the Milky Way and M31, there are estimated to be of the order $\sim 10^3$ SSSs, thus providing enough intrinsic emission at 10 Ryd compared to our constraints (e.g. Kahabka & van den Heuvel 1997). Taken at face value, our results would imply that most of the radiation produced by SSSs should escape from the ISM (in agreement with the results of Woods & Gilfanov 2016). As explored by Cantalupo (2010), the presence of such an intense radiation field at high energies has a profound impact on the cooling of the CGM and therefore on galaxy formation and evolution as we discuss in Section 6.

4.4. Collisional Ionization

Now we consider a non-dynamical gas which radiatively cools via collisions both in and out of equilibrium (CIE and CINE). These models are parameterized primarily by temperature. In the equilibrium case, the cooling efficiency is dependent upon the gas tempera-

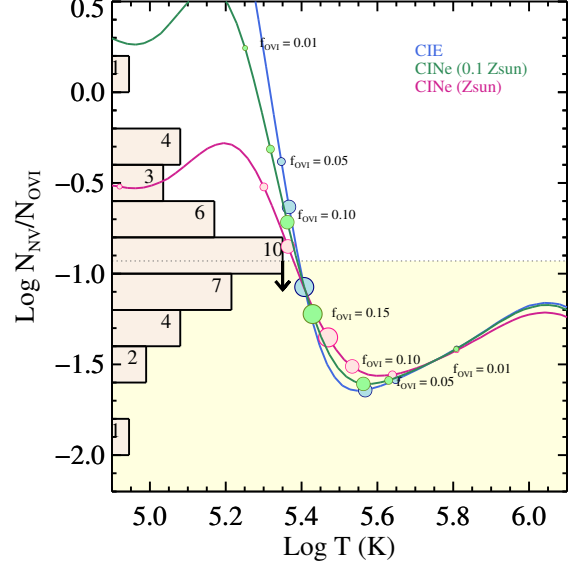


Figure 13. $\log N_{\text{NV}} / N_{\text{OVI}}$ as a function of gas temperature for collisionally-ionized gas both in (CIE) and out of equilibrium (CINE). The curves shown represent the models of Oppenheimer & Schaye (2013b), and the filled circles on each curve give the fraction of oxygen in the O VI state which varies with temperature. f_{OVI} is maximized close to the minimum allowed value of $\log N_{\text{NV}} / N_{\text{OVI}} \approx -1.5$. We show a histogram of the observed ratios for the individual components on the y-axis for reference, noting with the downward-facing arrow that the vast majority of these column density ratios are upper limits due to the non-detection of N V for the majority of the O VI components. The yellow-shaded area highlights the typical COS-Halos measured column density ratios of N V / O VI ≈ -0.93 . CIE and CINE models indicate that for the observed limits on $\log N_{\text{NV}} / N_{\text{OVI}}$, gas temperature lies within the range $5.4 < \log T < 5.6$ and the O VI gas fraction falls within $0.10 < f_{\text{OVI}} < 0.15$.

ture, density, and composition. In the absence of an additional heat source, the gas cools via the removal of electron kinetic energy due to recombinations with ions, collisional ionizations and excitations (followed shortly by line emission), and thermal bremsstrahlung. For non-equilibrium cooling, the gas is “overionized” compared to CIE because cooling is more rapid owing to a “recombination lag” (Gnat & Sternberg 2007).

Figure 13 shows $\log N_{\text{NV}} / N_{\text{OVI}}$ as a function of the gas temperature for collisionally-ionized gas both in (CIE; blue curve) and out of equilibrium (CINE; green and pink curves). On each curve, we supply the value of the fraction of oxygen in O VI predicted by the model. The observed N V/O VI ratios, represented on the y-axis as a histogram, require $T > 10^{5.35}$ K, which is approximately the temperature where the fraction of oxygen in O VI is maximal. One facet of the CIE and CINE models is that for $T > 10^{5.7}$ K, the fraction of oxygen in O VI drops so low that to reproduce the observed O VI column densities, one requires very high values of N_{O} that would imply metallicities above a few times solar. Thus, because of the shape of the cooling curve, CIE and CINE models require a very narrow range of temperature to reproduce the observations. The upper limits to the N V/O VI ratios are broadly consistent with this temperature range, and therefore are reproduced by a variety of collisional ionization models.

4.5. Complex Non-Equilibrium Models

Finally, we consider other ionization mechanisms to reproduce the observed O VI. These models are primarily a series of collisional ionization processes out of equilibrium. They were introduced first in the context of highly ionized gas detected within the Galactic halo, including gas associated with HVCs (Shapiro & Field 1976). Following previous work, we consider the predictions for a wide range of parameter space given by each model.

4.5.1. Radiative Cooling Flow

As shown in Figure 8, a radiative cooling flow model can give rise to a correlation between $N_{\text{O VI}}$ and its Doppler b parameter under the assumption that the b -value reflects a flow velocity (Edgar & Chevalier 1986). Wakker et al. (2012) describe in detail the model first proposed by Shapiro & Moore (1976) and later developed by Edgar & Chevalier (1986); Shapiro & Benjamin (1991) and Benjamin (1994). This model allows gas to cool via collisions as it moves at a constant speed. For a range of flow velocities ($v_{\text{flow}} < 30 \text{ km s}^{-1}$), the model tends to give narrow ranges of $\log N_{\text{V/O VI}}$ between -1.25 and -1.0 , and $\log \text{Si IV/O VI}$ of -1.9 to -0.2 (see also Wakker et al. 2012 for a discussion of this model). We note that nearly all of the observed Si IV is generated by photoionization from the warmer, upstream O VI-producing gas. Such self-photoionizing radiation may be problematic in a cosmological context, however, which we discuss in Section 6. Furthermore, this model does not include radiation from the EUVB. The gas bearing N V and O VI is cooling via collisional ionization at $T \approx 10^{5.5} \text{ K}$.

While the ratios predicted by the radiative cooling flow model are remarkably consistent with the COS-Halos intermediate and high-ion data, the results remain inconclusive with respect to $N_{\text{O VI}}$ and line-of-sight kinematics. The one-dimensional cooling flow model of Shapiro & Benjamin (1991) was calculated solely in the case of observing the gas from the Milky-Way, and thus only along the direction of the flow. Although $\log N_{\text{O VI}}$ is 14.5 in this geometry, consistent with the data, it is clear that the angle between the line of sight and the flow direction will impact the predicted column densities, and drive them down considerably.

4.5.2. Turbulent Mixing Layers

First proposed by Begelman & Fabian (1990), later developed by Slavin et al. (1993), and expanded upon by Kwak & Shelton (2010), the turbulent mixing layer model involves cool clouds moving through a hot medium possess a shell of gas at their boundary in which Kelvin-Helmholtz instabilities are mixing the hot and cool gas¹⁶. This turbulent mixing produces gas in the shell with an intermediate temperature, characterized by highly ionized species. This model is referred to as a turbulent mixing layer (TML), and is commonly invoked to explain the ionization state of Milky Way HVCs (Sembach et al. 2003; Fox et al. 2004; Wakker et al. 2012; Savage et al. 2014), and intergalactic intervening absorption (Tripp et al. 2008). Here, we consider the predicted column density ratios given by Slavin et al. (1993); Kwak & Shelton (2010), which are generally a function of two variables: the turbulent velocity, v_{turb} , which is allowed

to range from $25 - 100 \text{ km s}^{-1}$, and the mixing layer temperature, T_{mix} , which ranges from $10^{5.0} - 10^{5.5} \text{ K}$. The update by Kwak & Shelton (2010) includes a more detailed treatment of non-equilibrium ionization in a two-dimensional hydrodynamical model which has a small effect on the ratios, and a more significant effect on the total column densities. The resultant $N_{\text{V/O VI}}$ ranges from $-1 - -0.4$. However, the typical $N_{\text{O VI}}$ in Slavin et al. (1993) is $\sim 10^{12} \text{ cm}^{-2}$, requiring more than 300 such interfaces to exist along the line of sight to match the observed $N_{\text{O VI}}$ ($\sim 10^{14.5} \text{ cm}^{-2}$). In the Kwak & Shelton (2010) model, the average line of sight $N_{\text{O VI}}$ increases to $10^{12.8} \text{ cm}^{-2}$, easing the requirement for the number of clouds along each line of sight to be ~ 50 to match the COS-Halos O VI column densities. Nonetheless, this physical picture is difficult to reconcile with the observed absorption profiles, which show an average of 2.4 components per line of sight over a fairly narrow range of velocity.

4.5.3. Conductive Interfaces

A cool cloud embedded in a hot medium can also produce a surface layer in which cool gas is evaporating and hot gas is condensing because electron collisions are conducting heat between the two media (Borkowski et al. 1990; Gnat et al. 2010). Referred to as conductive interfaces, these models predict how the column densities of transition temperature ions change as a function of time and the angle between the magnetic field and the conduction layer orientation. Along magnetic field lines, the thermal conductivity of the interface is much greater, increasing the column densities of the high-ions. The thermal conduction at the interface layer may prevent formation of Kelvin-Helmholtz instabilities at the cloud-corona interface, ultimately leading to long cloud survival times (Armillotta et al. 2016). Before 2×10^5 years, the high-ion column densities change rapidly, and then stay relatively constant for the next ~ 5 Myrs. As Wakker et al. (2012) points out, this rapid evolution results in a unique value of the predicted ion ratios for 90% of the lifetime of the interface. The updated conductive interface models of Gnat et al. (2010) include a range of temperature and pressure of the surrounding hot medium of $10^6 - 10^7 \text{ K}$, and $0.1 - 50 \text{ K cm}^{-3}$, respectively. They also include photoionization by the EUVB. Wakker et al. (2012) have found that the expanded parameter space of the updated models changes the predicted column densities by an average of 0.2 dex from the original Borkowski et al. (1990) results.

Conductive interfaces can have $\log N_{\text{V/O VI}}$ as low as -1.25 for B_{\parallel} and -1.0 for B_{\perp} . The ratio $\log \text{Si IV/O VI}$ is -2.0 for B_{\parallel} and -1.2 for B_{\perp} . These ratios are consistent with many of the COS-Halos data points. Yet, in these models the column density of O VI never exceeds 10^{13} cm^{-2} (Gnat et al. 2010), requiring $20 - 100$ interfaces along each line of sight for consistency with the absorption-line data. For different model parameters (i.e. hot medium with $T < 10^7 \text{ K}$), $N_{\text{O VI}}$ can be as low as 10^{10} cm^{-2} , and tens of thousands of interfaces are required to bring the model and data to consistency. Thus, we reach a similar conclusion with respect to conductive interfaces as we did for turbulent mixing layers. There is simply not enough total column density of high ions

¹⁶ This relation can also give rise to an N-b relationship

produced in this model for it to be a plausible explanation for the abundance of O VI absorption observed in the halos of star-forming galaxies.

4.5.4. Supersonic Shocks

Another way to produce a significant amount of O VI absorption is to consider collisionally ionized gas behind a high speed radiative shock (Dopita & Sutherland 1996; Heckman et al. 2002; Allen et al. 2008; Gnat & Sternberg 2009; Grimes et al. 2009).¹⁶ Under the assumption of a steady, one-dimensional flow, and a given metallicity, several models predict column densities of high ions in the post-shock cooling layers. A generic feature of these models is that $N_{\text{O VI}}$ in the post-shock gas stays below $\sim 10^{12} \text{ cm}^{-2}$ for $v_{\text{shock}} < 150 \text{ km s}^{-1}$, and then abruptly increases by two orders of magnitude at $v_{\text{shock}} = 175 \text{ km s}^{-1}$. Here we use the results of Allen et al. (2008) who produce tables that are valid for solar metallicity, shock speeds that range from $100 - 1000 \text{ km s}^{-1}$ and pressure exerted by the transverse magnetic field ($Bn^{-\frac{1}{2}}$) ranging from $10^{-4} \mu\text{G cm}^{-3/2} - 10 \mu\text{G cm}^{-3/2}$. The magnetic pressure is important because it limits the compression through the shock, and thus higher magnetic parameters produce higher $N_{\text{O VI}}$. We consider the full model range for the magnetic parameter of the gas. Gnat & Sternberg (2009) has updated these models for a wider range of metallicity, though they only consider faster shocks with v_{shock} of 600 and 2000 km s^{-1} .

Generally, $N_{\text{O VI}}$ remains at some level for the first $\sim 3 \text{ Myr}$ after the initial shock, and then abruptly increases to by two orders of magnitude during the non-equilibrium cooling phase. The total $N_{\text{O VI}}$ in the post-shock gas can range from $10^{14.3} \text{ cm}^{-2}$ to $10^{15.4} \text{ cm}^{-2}$ for weak magnetic pressure to strong magnetic pressure over the range of velocities considered. N V has a similar broad range, though is consistently $1 - 1.5 \text{ dex}$ lower than the total $N_{\text{O VI}}$, consistent with the COS-Halos data. The kinematics of O VI in this model would likely be varied and complex depending on shock speed, as is observed. And furthermore, if these supersonic shocks arise as a result of starburst-driven winds, this model provides a natural explanation for the correlation between $N_{\text{O VI}}$ of the ‘broad’ O VI absorbers and the SFR/R^2 . Thus, collisionally-ionized gas cooling behind a fast shock remains a viable physical model for the observed O VI, and we consider its broader implications for gas kinematics and cooling times in the discussion.

5. SUMMARY OF RESULTS

We have analyzed the O VI kinematics and column densities along 24 lines of sight probing the halos of low-redshift, $L \sim L^*$ star-forming galaxies at one-dimensional projected distances of $15 - 150 \text{ kpc}$. We present a simple, data-driven method of identifying three distinct O VI kinematic subtypes present in the *HST*/COS FUV spectra, which we enumerate below. Each kinematic subtype shows different behavior with respect to its total column density and host galaxy properties like SFR, R , and M_{halo} . For the majority of O VI absorbers in L^* galaxy halos, regardless of their kinematic subtype, photoionization by the EUVB-only is strongly disfavored due to the implied path lengths $> 100 \text{ kpc}$. Furthermore, for every kinematic subtype, upper limits to $N_{\text{N V}}/N_{\text{O VI}}$

place strong constraints on the physical state of the gas under the conditions of photo and collisional ionization. Finally, we infer that there are multiple distinct physical processes that lead to the observed widespread O VI in the CGM of star-forming galaxies.

The salient observed properties of the three kinematic subtypes are:

1. The ‘no-low’ type absorbers (8/39) are typically broad ($b \approx 50 \text{ km s}^{-1}$) O VI absorption lines with no underlying, detectable absorption from lower ionization state metal species. These 8 absorbers follow a statistically significant, fairly tight correlation between their column density and line-widths, consistent with predictions for radiatively cooling gas in which the total column density is set by a characteristic cooling flow velocity (e.g. gas cooling behind a shock, Dopita & Sutherland 1996; mixing turbulently in a fixed layer between cool and hot gas, Begelman & Fabian 1990; collapsing in a cooling instability, Heckman et al. 2002). The upper limits on $N_{\text{N V}}/N_{\text{O VI}}$ strongly suggest a gas temperature of $T \approx 10^{5.5} \text{ K}$ under the assumption of collisional ionization. *These ‘no-low’ type absorbers are found strictly in the COS-Halos galaxies with $10^{11.5} < M_{\text{halo}} < 10^{12} M_{\odot}$, where the halo virial temperature is also $T \approx 10^{5.5} \text{ K}$.*
2. The ‘broad’ type O VI absorbers ($b \gtrsim 40 \text{ km s}^{-1}$) that are coincident with relatively narrow low-ion absorbers are the most common kinematic subtype found in the CGM of star-forming galaxies (16/39). These ‘broad’ type absorbers alone set the observed trends between $N_{\text{O VI}}$ and galaxy properties (R , SFR), and dominate the total column density along each line of sight. They are significantly broader than the lower column density O VI lines seen in samples of absorbers observed along blindly selected lines-of-sight (i.e. in the IGM). Their total columns and line-widths are not inconsistent with the radiative cooling relation between $\log N$ and b , but these absorbers could be impacted by the blending of several narrow components separated by $v < 10 \text{ km s}^{-1}$. The upper limits on $N_{\text{N V}}/N_{\text{O VI}}$ strongly rule out most photoionization models, both in and out of equilibrium, both with and without steep density gradients that include radiation from the EUVB only. We use the upper limits of $N_{\text{N V}}/N_{\text{O VI}}$ to estimate the total required intensity in addition to that of the EUVB, and find that it must exceed the EUVB by a factor of 100 at energies $> 10 \text{ Rydberg}$ for photoionization to remain relevant for producing the observed O VI. The upper limits to $N_{\text{N V}}/N_{\text{O VI}}$ are consistent with collisional ionization models (in and out of equilibrium), where the fraction of oxygen in O VI is maximized, $T \approx 10^{5.5} \text{ K}$.
3. The ‘narrow’ type O VI absorbers ($b \approx 25 \text{ km s}^{-1}$) that are consistent with low-ion absorbers represent 15/39, or 38%, of the O VI components in the CGM; they are perhaps the most puzzling kinematic subtype. Their total columns and line-widths are *inconsistent with the radiative cooling*

correlation between $\log N$ and b , as they systematically lie above it by 0.2 - 0.4 dex. Their column densities do not correlate with *any* galaxy property observed by COS-Halos. Furthermore, upper limits on $N_{\text{NV}}/N_{\text{OVI}}$ strongly disfavor an origin in gas photoionized by the EUVB. Although upper limits on $N_{\text{NV}}/N_{\text{OVI}}$ give $T_{\text{CIE}} \approx 10^{5.4}$ K, for collisional ionization models, it is not clear how such models could give the observed tight kinematic correspondence between low and high ionization state gas, i.e. produce O VI line widths generally consistent with those of the low-ionization state material.

6. DISCUSSION

Our work shows that even in the relatively well-controlled environment of $z \sim 0.2$ star-forming, L^* galaxy halos at $R < 150$ kpc, the highly-ionized O VI-bearing gas appears to have a variety of origins and a range of ionization states. This result may explain why previous works have been unable to come to a generic conclusion about the origin of O VI (but see: Heckman et al. 2002; Bordoloi et al. 2016). The present study builds on those previous efforts which laid the foundation for the emerging complex picture of highly ionized, diffuse gas in a wide range of environments at a wide range of redshifts (e.g. Sembach et al. 2003; Fox et al. 2004; Tumlinson et al. 2005; Fox et al. 2006; Tripp et al. 2008; Fox et al. 2009; Lehner et al. 2009; Wakker & Savage 2009; Narayanan et al. 2010, 2011; Lehner et al. 2011; Prochaska et al. 2011b; Savage et al. 2011; Muzahid et al. 2012; Wakker et al. 2012; Narayanan et al. 2012; Savage et al. 2014; Lehner et al. 2014; Hussain et al. 2015). Simply, there is no single model that can self-consistently explain the observed variety of O VI kinematic correspondence with low-ionization state gas along with the high-ion absorption-line component column density ratios.

In this Section, we focus on favored physical and/or phenomenological explanations for each of the distinct kinematic subtypes. We comment on their implications for the total baryonic contribution of O VI-bearing gas to the galaxy halo, discuss gas cooling times, and halo dynamics.

6.1. The ‘No-Low’ Absorbers: $T \approx T_{\text{vir}}$ Gas

The theory that there exists a ‘critical’ galaxy halo mass marking a sharp transition in gas cooling rates has persisted since the early days of analytic galaxy formation models (Rees & Ostriker 1977; Silk 1977; Binney 1977), and been refined by modern cosmological hydrodynamical simulations (e.g. Kereš et al. 2005; Stinson et al. 2015; Oppenheimer et al. 2016). Generally, galaxies with $M_{\text{halo}} < M_{\text{crit}}$ are able to accrete cool gas onto their disks, while the accreting gas in galaxies with $M_{\text{halo}} > M_{\text{crit}}$ shock heats to the virial temperature, and cools over a dynamical time. However, it is now widely recognized by theorists that feedback plays a key role in the regulation of the halo gaseous medium, and the physics of the gas both above and below the critical halo mass threshold (e.g. Oppenheimer & Davé 2008; Governato et al. 2010; Faucher-Giguère & Kereš 2011; Hopkins et al. 2014; Nelson et al. 2015; Muratov et al. 2015; Fielding et al. 2016; Christensen et al. 2016; Oppenheimer et al. 2016).

One of the key discoveries of our kinematic study is that the ‘no-low’ kinematic subtype of O VI absorption abruptly disappears for galaxies with $M_{\text{halo}} > 10^{12} M_{\odot}$. This break has a statistical significance of 3σ for the 8 ‘no-low’ data points, and is not likely the result of a selection effect. This sharp mass cut-off appears to be consistent with the critical halo mass below which $T_{\text{vir}} \approx 10^{5.5}$ K (Oppenheimer et al. 2016). We showed that the no-low O VI absorber is most likely collisionally ionized, by noting its remarkable consistency with radiative cooling predictions (for a wide range of physical scenarios) for an N - b relation, and that its limits on $N_{\text{NV}}/N_{\text{OVI}}$ are consistent with collisional ionization models for $T \approx 10^{5.5}$ K. We note that the density of this gas must be $\lesssim 2 \times 10^{-5} \text{ cm}^{-3}$ for the cooling time to be $> 10^9$ years in CIE models, and hence for gas not to be in dynamical state (calculated at $Z = 0.1Z_{\odot}$; Gnat & Sternberg 2007; Oppenheimer & Schaye 2013b). The simplest interpretation of this result is that the ‘no-low’ O VI absorbers are tracing virialized halo gas in the subset of COS-Halos galaxies with $M_{\text{halo}} < 10^{12} M_{\odot}$.

Although the gas is most likely bound to the galaxy halo (See Figure 9), the large distribution of the ‘no-low’ velocity centroids with respect to the galaxy systemic velocity (Δv) is not obviously consistent with well-behaved virialized gas supported by thermal pressure in a hydrostatic halo. In a complementary analysis of O VI absorption in 14 mostly sub- L^* halos, Mathes et al. (2014) find a mass dependence for O VI kinematics. In their study, the velocities of O VI absorbers relative to the galaxy systemic velocities are much higher for galaxies with $M_{\text{halo}} < 10^{11.5} M_{\odot}$. There are several possibilities for such a large dispersion in velocities. For example, in Oppenheimer et al. (2016) the O VI-bearing gas traces extended $T \sim 10^{5.5}$ K gas mostly between $1 - 2 R_{\text{vir}}$ around such halos, which would provide such a kinematic offset.

Additionally, Fielding et al. (2016) present an idealized, three-dimensional hydrodynamic calculation in which they explore the intertwined roles of cosmological gas accretion and large-scale, cooling galactic winds for three fiducial halos at 10^{11} , $10^{11.5}$, and $10^{12} M_{\odot}$. The gas properties in the lower mass halos are considerably more affected by the feedback from the galaxy. Below their critical mass ($10^{11.5} M_{\odot}$; offset from ours by 0.5 dex), Fielding et al. (2016) note that the cooling time of virialized gas is relatively short, and the halo gas is largely supported by turbulence and ram pressure generated from the vigorous feedback instead of the more typical thermal pressure thought to support virialized halos with $M_{\text{halo}} > 10^{12} M_{\odot}$. The turbulence would impact the line widths, and the large-scale motions would induce a sloshing of gas in the halo that could produce large velocity offsets from the galaxy systemic velocity. Such a picture may help to explain why the $|\Delta v| > 100 \text{ km s}^{-1}$ for the ‘no-low’ O VI absorbers in the lower mass halos. Future studies by both observers and theorists should explore the kinematics of virialized gas in halos with masses $< 10^{12} M_{\odot}$.

The mean N_{OVI} for the ‘no-low’ absorbers is $10^{14.2} \text{ cm}^{-2}$ (compared to $10^{14.5} \text{ cm}^{-2}$ for the ‘broad’ O VI absorbers). Their ratios $N_{\text{NV}}/N_{\text{OVI}}$ indicate that O VI represents 15% of all the oxygen in this gas (Figure 13), implying a total column, $N_{\text{O}} = 10^{15} \text{ cm}^{-2}$. We follow the

simple formulation by (e.g. Tumlinson et al. 2011; Werk et al. 2014) of turning a column density into a mass surface density in order to find the total mass of the ‘virialized’ halo gas. We allow the gas to have a metallicity between solar and a tenth solar (Asplund et al. 2009). Assuming this gas fills the 150 kpc radius of the low-mass subset of COS-Halos galaxies, we find $M_{\text{gas}} \approx 10^{9-10} M_{\odot}$, where the higher value corresponds to the lower metallicity. For a halo mass of $10^{11.5} M_{\odot}$ that has its full cosmological share of baryons ($\sim 17\%$), this mass represents anywhere between 5 and 50% of the galaxy halo baryons. We note that in the Fielding et al. (2016) model, this virial temperature gas is cooling rapidly, which results in a complete loss of thermal pressure support, which leads to dramatic winds and subsequent cooling shocks at $T \approx T_{\text{vir}}$. In contrast, the model presented by Oppenheimer et al. (2016) can account for the ‘no-low’ absorbers with a low-density, $\sim 10^{5.5}$ K substrate mainly at $1 - 2 R_{\text{vir}}$ that has cooling times comparable to the Hubble time.

6.2. Photoionization by Local Sources

The measured upper limits on the ratio $N_{\text{NV}}/N_{\text{OVI}}$ in the highly ionized gas strongly disfavor origin of O VI in gas photoionized by the EUVB only for all kinematic subtypes. To emphasize this point, we constructed a toy model including a black-body radiation component from local sources and found that luminosities with values $\nu L_{\nu} > 10^{40} \text{ erg s}^{-1}$ at ~ 10 Ryd should be produced by our galaxies in order to match the data. This value corresponds to radiation exceeding the level supplied by the EUVB by a factor of 100 at energies above 10 Rydberg for a gas density of $\log n_{\text{H}} = -3.5 \text{ cm}^{-3}$. In this phenomenology, O VI is under-abundant around non star-forming galaxies because there are not enough high energy photons escaping from the disk of the galaxy to ionize oxygen into O VI. A major implication of this model is that the dramatic release of these high energy photons from the disk photoionizes the primary coolants of the halo gas, thus increasing the cooling time of the gas by up to two orders of magnitude (Cantalupo 2010). In other words, photoionization from local sources in the galaxy (distinct from SN feedback) would then strongly regulate the rate at which galaxies acquire their gas. This model additionally requires a vast revision of the standard model where quasars dominate the EUVB at ~ 10 Ryd.

We explored which sources of radiation may be viable candidates and found that both the hot ISM heated by supernovae and supersoft X-ray sources (SSSs) may produce sufficient high energy radiation at large R , ~ 2 orders of magnitude larger than the EUVB at high energies. Future studies will address how to better constrain the shape and intensity, and thus the physical origin of the required radiation field. There are two benefits of this model: smaller OVI path lengths and SFR/R^2 correlation is explained. However, several challenges face the model. For one, the implied extra radiation has dramatic implications on the EUVB itself. Geometric considerations and the assumption that the ionizing emissions from the associated galaxy trace star formation or stellar mass prohibits more than an order unity enhancement at > 100 kpc in proximity radiation over the background at all wavelengths (Miralda-Escudé 2005, Upton Sanderbeck et al. in prep). Furthermore, this model cannot easily explain the diversity of low and high ion corre-

spondence, seen in both the ‘narrow’ and ‘broad’ O VI.

6.3. Shocks and Radiatively Cooling Gas Behind Fast Winds

Galaxy-scale winds are a natural model to address for the CGM, especially given their observed ubiquity in star-forming galaxies (e.g. Martin et al. 2012; Rubin et al. 2014) and their potential to scale with SFR/R^2 (Borthakur et al. 2013). Recently, Thompson et al. (2016) presented a detailed picture in which initially hot, adiabatic outflows radiatively cool on large scales (~ 100 kpc) and timescales less than a Hubble time. These winds directly give rise to cool, photoionized gas clouds that precipitate out (see also: Wang 1995; Efstathiou 2000). This analytical model solves several problems relating to the CGM gas. In particular, it does not require that the cool gas be in pressure equilibrium with a virialized hot halo, consistent with observations that seem to rule this pressure-equilibrium out Werk et al. (2014). Because the cool $\sim 10^4$ K clouds arise from the radiatively cooling gas bearing O VI, we would expect their velocities to be similar. This physical scenario would likely give rise to a range of observed velocities and line-widths, depending on impact parameter, evolutionary stage of the wind, and the angle of viewing the shocked and post-shocked material. We consider this model promising, but must await its predictions on the kinematic signatures one might observe in low and high ionization state gas before coming to a conclusion on its consistency with observations.

7. CONCLUSIONS

Conclusions regarding the origin and fate of circumgalactic gas are inextricably linked to the initial assumptions we make about the physical processes that determine its ionization state. In this work we have demonstrated that the kinematics of the highly-ionized gas in addition to gas column density ratios, contain a wealth of information useful for constraining physical models of the CGM. We have examined a number of equilibrium and non-equilibrium ionization models that predict gas characterized by strong O VI absorption. The constraints from the COS-Halos absorption-line column density and kinematics measurements strongly disfavor many of the models considered. At least some fraction of O VI appears to represent halo gas at the virial temperature, while most of the total column of O VI may result from either gas photoionized primarily by local high-energy sources or gas radiatively cooling on large scales behind a multiphase, fast wind. The latter two models imply very different ionization states and physical origins for the gas. Each model has its own set of strengths and weaknesses.

Successful models of the CGM must account for: (1) the velocity correspondence between the low-ionization state, photoionized gas and the O VI absorption; (2) O VI column densities $\gtrsim 10^{14} \text{ cm}^{-2}$ and highly variable line widths, $10 \text{ km s}^{-1} < b < 100 \text{ km s}^{-1}$; and (3) the absence of O VI around non-star-forming galaxies and related tight correspondence between N_{OVI} and SFR/R^2 . For photoionization models to progress, future studies must focus on a detailed treatment of both the origin and long-term survival of these richly structured clouds

and the sources of ionizing radiation. A different issue faces the analytic, phenomenological, and hydrodynamical models that generate significant O VI by collisional ionization. These models often provide a highly detailed physical treatment of the gas dynamics, origin, and ionization state, but make limited predictions with respect to the full range of possible observational measurements. Future insight on the origins of O VI will come from comparing detailed observational analyses of gas kinematics with the model predictions for the line-of-sight kinematics.

8. ACKNOWLEDGEMENTS

Support for this work was provided by NASA through program GO11598, and through Hubble Fellowship grant # 51332 from the Space Telescope Science Institute, which is operated by the Association of Universities for Research in Astronomy, Inc., under NASA contract NAS 5-26555. B. Oppenheimer's contributions to this work are supported through the NASA ATP14-0142 grant. SC gratefully acknowledges support from Swiss National Science Foundation grant PP00P2_163824. JKW acknowledges the Esalen Institute for providing a stunningly beautiful setting for writing a large portion of the text. The authors sincerely thank Blair Savage who provided thorough and insightful referee reports that significantly improved the paper. Specifically, he encouraged the detailed kinematic analysis, which was largely absent from the initially-submitted version of this paper. JKW would like to especially thank Jonathan Stern, Rongmon Bordoloi, Renyue Cen, Charles Danforth, Joe Hennawi, Sowgat Muzahid, Brian O'Shea, Paul Shapiro, Todd Thompson, Julianne Dalcanton, Sarah Tuttle, and Evgenii Vasiliev, for very useful exchanges regarding ionization processes, pressure-support in galaxy halos, and O VI in general. Additionally, JKW would like to acknowledge UW graduate student Hannah Bish for her helpful suggestion of the term 'no-low.'

Facilities: HST: COS Keck: LRIS Magellan: Mage

REFERENCES

- Allen, M. G., Groves, B. A., Dopita, M. A., Sutherland, R. S., & Kewley, L. J. 2008, *ApJS*, 178, 20
- Armillotta, L., Werk, J. K., Prochaska, J. X., Fraternali, F., & Marinacci, F. 2016, *ArXiv e-prints*, arXiv:1608.05416
- Asplund, M., Grevesse, N., Sauval, A. J., & Scott, P. 2009, *ARA&A*, 47, 481
- Battisti, A. J., Meiring, J. D., Tripp, T. M., et al. 2012, *ApJ*, 744, 93
- Begelman, M. C., & Fabian, A. C. 1990, *MNRAS*, 244, 26P
- Benjamin, R. A. 1994, PhD thesis, THE UNIVERSITY OF TEXAS AT AUSTIN.
- Binney, J. 1977, *ApJ*, 215, 483
- Blanton, M. R., Brinkmann, J., Csabai, I., et al. 2003, *AJ*, 125, 2348
- Bordoloi, R., Heckman, T. M., & Norman, C. A. 2016, *ArXiv e-prints*, arXiv:1605.07187
- Borkowski, K. J., Balbus, S. A., & Frisstrom, C. C. 1990, *ApJ*, 355, 501
- Borthakur, S., Heckman, T., Strickland, D., Wild, V., & Schiminovich, D. 2013, *ApJ*, 768, 18
- Bowen, D. V., Jimenez, R., Jenkins, E. B., & Pettini, M. 2001, *ApJ*, 547, 39
- Burchett, J. N., Tripp, T. M., Prochaska, J. X., et al. 2015, *ApJ*, 815, 91
- Cantalupo, S. 2010, *MNRAS*, 403, L16
- Cen, R. 2013, *ApJ*, 770, 139
- Cen, R., & Safarzadeh, M. 2016, *ArXiv e-prints*, arXiv:1609.03583
- Cerviño, M., Mas-Hesse, J. M., & Kunth, D. 2002, *A&A*, 392, 19
- Chen, H.-W., & Mulchaey, J. S. 2009, *ApJ*, 701, 1219
- Christensen, C. R., Davé, R., Governato, F., et al. 2016, *ApJ*, 824, 57
- Churchill, C. W., Vander Vliet, J. R., Trujillo-Gomez, S., Kacprzak, G. G., & Klypin, A. 2015, *ApJ*, 802, 10
- Danforth, C. W., Keeney, B. A., Tilton, E. M., et al. 2016, *ApJ*, 817, 111
- Davé, R., Hernquist, L., Katz, N., & Weinberg, D. H. 1999, *ApJ*, 511, 521
- Davé, R., & Tripp, T. M. 2001, *ApJ*, 553, 528
- Dopita, M. A., & Sutherland, R. S. 1996, *ApJS*, 102, 161
- Edgar, R. J., & Chevalier, R. A. 1986, *ApJ*, 310, L27
- Efstathiou, G. 2000, *MNRAS*, 317, 697
- Faerman, Y., Sternberg, A., & McKee, C. F. 2016, *ArXiv e-prints*, arXiv:1602.00689
- Faucher-Giguère, C.-A., & Kereš, D. 2011, *MNRAS*, 412, L118
- Ferland, G. J., Porter, R. L., van Hoof, P. A. M., et al. 2013, *RMxAA*, 49, 137
- Fielding, D., Quataert, E., McCourt, M., & Thompson, T. A. 2016, *ArXiv e-prints*, arXiv:1606.06734
- Ford, A. B., Werk, J. K., Davé, R., et al. 2016, *MNRAS*, 459, 1745
- Fox, A. J., Prochaska, J. X., Ledoux, C., et al. 2009, *A&A*, 503, 731
- Fox, A. J., Savage, B. D., & Wakker, B. P. 2006, *ApJS*, 165, 229
- Fox, A. J., Savage, B. D., Wakker, B. P., et al. 2004, *ApJ*, 602, 738
- Fox, A. J., Wakker, B. P., Savage, B. D., et al. 2005, *ApJ*, 630, 332
- Fox, A. J., Lehner, N., Tumlinson, J., et al. 2013, *ApJ*, 778, 187
- Froning, C. S., & Green, J. C. 2009, *Ap&SS*, 320, 181
- Ghavamian, P., Aloisi, A., Lennon, D., et al. 2009, Preliminary Characterization of the Post-Launch Line Spread Function of COS, Tech. rep.
- Gnat, O., & Sternberg, A. 2007, *ApJS*, 168, 213
- . 2009, *ApJ*, 693, 1514
- Gnat, O., Sternberg, A., & McKee, C. F. 2010, *ApJ*, 718, 1315
- Governato, F., Brook, C., Mayer, L., et al. 2010, *Nature*, 463, 203
- Green, J. C., Froning, C. S., Osterman, S., et al. 2012, *ApJ*, 744, 60
- Greiner, J. 2000, *NA*, 5, 137
- Grimes, J. P., Heckman, T., Aloisi, A., et al. 2009, *ApJS*, 181, 272
- Haardt, F., & Madau, P. 2001, in *Clusters of Galaxies and the High Redshift Universe Observed in X-rays*, ed. D. M. Neumann & J. T. V. Tran
- Haardt, F., & Madau, P. 2012, *ApJ*, 746, 125
- Heckman, T. M., Norman, C. A., Strickland, D. K., & Sembach, K. R. 2002, *ApJ*, 577, 691
- Henry, R. B. C. 1993, *MNRAS*, 261, 306
- Hopkins, P. F., Kereš, D., Oñorbe, J., et al. 2014, *MNRAS*, 445, 581
- Howk, J. C., Ribaud, J. S., Lehner, N., Prochaska, J. X., & Chen, H.-W. 2009, *MNRAS*, 396, 1875
- Hummels, C. B., Bryan, G. L., Smith, B. D., & Turk, M. J. 2013, *MNRAS*, 430, 1548
- Hussain, T., Muzahid, S., Narayanan, A., et al. 2015, *MNRAS*, 446, 2444
- Jenkins, E. B., Bowen, D. V., Tripp, T. M., & Sembach, K. R. 2005, *ApJ*, 623, 767
- Johnson, S. D., Chen, H.-W., & Mulchaey, J. S. 2015, *MNRAS*, 449, 3263
- Kahabka, P., & van den Heuvel, E. P. J. 1997, *ARA&A*, 35, 69
- Kereš, D., Katz, N., Weinberg, D. H., & Davé, R. 2005, *MNRAS*, 363, 2
- Kwak, K., Henley, D. B., & Shelton, R. L. 2011, *ApJ*, 739, 30
- Kwak, K., & Shelton, R. L. 2010, *ApJ*, 719, 523
- Lehner, N., O'Meara, J. M., Fox, A. J., et al. 2014, *ApJ*, 788, 119
- Lehner, N., Prochaska, J. X., Kobulnicky, H. A., et al. 2009, *ApJ*, 694, 734
- Lehner, N., Zech, W. F., Howk, J. C., & Savage, B. D. 2011, *ApJ*, 727, 46
- Lehner, N., Howk, J. C., Tripp, T. M., et al. 2013, *ApJ*, 770, 138
- Leitherer, C., Schaerer, D., Goldader, J. D., et al. 1999, *ApJS*, 123, 3
- Liang, C. J., Kravtsov, A. V., & Agertz, O. 2016, *MNRAS*, 458, 1164
- Martin, C. L., Shapley, A. E., Coil, A. L., et al. 2012, *ApJ*, 760, 127

- Mathes, N. L., Churchill, C. W., Kacprzak, G. G., et al. 2014, *ApJ*, 792, 128
- Meiring, J. D., Tripp, T. M., Werk, J. K., et al. 2013, *ApJ*, 767, 49
- Mineo, S., Gilfanov, M., & Sunyaev, R. 2012, *MNRAS*, 426, 1870
- Miralda-Escudé, J. 2005, *ApJ*, 620, L91
- Moster, B. P., Somerville, R. S., Maulbetsch, C., et al. 2010, *ApJ*, 710, 903
- Muratov, A. L., Kereš, D., Faucher-Giguère, C.-A., et al. 2015, *MNRAS*, 454, 2691
- Muzahid, S., Kacprzak, G. G., Churchill, C. W., et al. 2015, *ApJ*, 811, 132
- Muzahid, S., Srianand, R., Bergeron, J., & Petitjean, P. 2012, *MNRAS*, 421, 446
- Narayanan, A., Savage, B. D., & Wakker, B. P. 2012, *ApJ*, 752, 65
- Narayanan, A., Wakker, B. P., Savage, B. D., et al. 2010, *ApJ*, 721, 960
- Narayanan, A., Savage, B. D., Wakker, B. P., et al. 2011, *ApJ*, 730, 15
- Nelson, D., Genel, S., Vogelsberger, M., et al. 2015, *MNRAS*, 448, 59
- Oppenheimer, B. D., & Davé, R. 2008, *MNRAS*, 387, 577
- . 2009, *MNRAS*, 395, 1875
- Oppenheimer, B. D., & Schaye, J. 2013a, *MNRAS*, 434, 1063
- . 2013b, *MNRAS*, 434, 1043
- Oppenheimer, B. D., Crain, R. A., Schaye, J., et al. 2016, *MNRAS*, 460, 2157
- Pachat, S., Narayanan, A., Muzahid, S., et al. 2016, *MNRAS*, 458, 733
- Peebles, M. S., Werk, J. K., Tumlinson, J., et al. 2014, *ApJ*, 786, 54
- Prochaska, J. X. 1999, *ApJ*, 511, L71
- Prochaska, J. X., Henry, R. B. C., O’Meara, J. M., et al. 2002, *PASP*, 114, 933
- Prochaska, J. X., Weiner, B., Chen, H.-W., Cooksey, K. L., & Mulchaey, J. S. 2011a, *ApJS*, 193, 28
- . 2011b, *ApJS*, 193, 28
- Prochaska, J. X., Hennawi, J. F., Lee, K.-G., et al. 2013, *ApJ*, 776, 136
- Rahmati, A., Schaye, J., Crain, R. A., et al. 2016, *MNRAS*, 459, 310
- Rees, M. J., & Ostriker, J. P. 1977, *MNRAS*, 179, 541
- Reimers, D., Vogel, S., Hagen, H.-J., et al. 1992, *Nature*, 360, 561
- Richter, P., Savage, B. D., Tripp, T. M., & Sembach, K. R. 2004, *ApJS*, 153, 165
- Rubin, K. H. R., Prochaska, J. X., Koo, D. C., et al. 2014, *ApJ*, 794, 156
- Savage, B. D., Kim, T.-S., Wakker, B. P., et al. 2014, *ApJS*, 212, 8
- Savage, B. D., Lehner, N., & Narayanan, A. 2011, *ApJ*, 743, 180
- Savage, B. D., Sembach, K. R., Tripp, T. M., & Richter, P. 2002, *ApJ*, 564, 631
- Savage, B. D., Sembach, K. R., Jenkins, E. B., et al. 2000, *ApJ*, 538, L27
- Sembach, K. R., Tripp, T. M., Savage, B. D., & Richter, P. 2004, *ApJS*, 155, 351
- Sembach, K. R., Wakker, B. P., Savage, B. D., et al. 2003, *ApJS*, 146, 165
- Shapiro, P. R., & Benjamin, R. A. 1991, *PASP*, 103, 923
- Shapiro, P. R., & Field, G. B. 1976, *ApJ*, 205, 762
- Shapiro, P. R., & Moore, R. T. 1976, *ApJ*, 207, 460
- Shen, S., Madau, P., Guedes, J., et al. 2013, *ApJ*, 765, 89
- Shull, J. M., Tumlinson, J., & Giroux, M. L. 2003, *ApJ*, 594, L107
- Silk, J. 1977, *ApJ*, 211, 638
- Slavin, J. D., Shull, J. M., & Begelman, M. C. 1993, *ApJ*, 407, 83
- Stern, J., Hennawi, J. F., Prochaska, J. X., & Werk, J. K. 2016, *ApJ*, 830, 87
- Stinson, G. S., Dutton, A. A., Wang, L., et al. 2015, *MNRAS*, 454, 1105
- Stocke, J. T., Keeney, B. A., Danforth, C. W., et al. 2013, *ApJ*, 763, 148
- . 2014, *ApJ*, 791, 128
- Suresh, J., Rubin, K. H. R., Kannan, R., et al. 2015, *ArXiv e-prints*, arXiv:1511.00687
- Thompson, T. A., Quataert, E., Zhang, D., & Weinberg, D. H. 2016, *MNRAS*, 455, 1830
- Tripp, T. M., Aracil, B., Bowen, D. V., & Jenkins, E. B. 2006, *ApJ*, 643, L77
- Tripp, T. M., Jenkins, E. B., Bowen, D. V., et al. 2005, *ApJ*, 619, 714
- Tripp, T. M., & Savage, B. D. 2000, *ApJ*, 542, 42
- Tripp, T. M., Sembach, K. R., Bowen, D. V., et al. 2008, *ApJS*, 177, 39
- Tripp, T. M., Meiring, J. D., Prochaska, J. X., et al. 2011a, *Science*, 334, 952
- . 2011b, *Science*, 334, 952
- Tumlinson, J., Shull, J. M., Giroux, M. L., & Stocke, J. T. 2005, *ApJ*, 620, 95
- Tumlinson, J., Thom, C., Werk, J. K., et al. 2011, *Science*, 334, 948
- . 2013, *ApJ*, 777, 59
- Vasiliev, E. O., Ryabova, M. V., & Shchekinov, Y. A. 2015, *MNRAS*, 446, 3078
- Wakker, B. P., & Savage, B. D. 2009, *ApJS*, 182, 378
- Wakker, B. P., Savage, B. D., Fox, A. J., Benjamin, R. A., & Shapiro, P. R. 2012, *ApJ*, 749, 157
- Wang, B. 1995, *ApJ*, 444, 590
- Werk, J. K., Prochaska, J. X., Thom, C., et al. 2012, *ApJS*, 198, 3
- . 2013, *ApJS*, 204, 17
- Werk, J. K., Prochaska, J. X., Tumlinson, J., et al. 2014, *ApJ*, 792, 8
- Woods, T. E., & Gilfanov, M. 2016, *MNRAS*, 455, 1770
- Zafar, T., Centurión, M., Molaro, P., et al. 2014, *Mem. Soc. Astron. Italiana*, 85, 363
- Zheng, Y., Putman, M. E., Peek, J. E. G., & Joung, M. R. 2015, *ApJ*, 807, 103